A Beam Trajectory Monitor using Spontaneous Undulator Radiation at the TTF-FEL

Johnny S.T. Ng

DESY, Notkestr. 85, 22603 Hamburg, Germany.

Abstract

A photon beam with brilliance many orders of magnitude higher than the existing synchrotron light sources can be generated in the VUV to the X-ray range via the Self Amplified Spontaneous Emission (SASE) mechanism with the single passage of an electron beam through a long undulator. Critical to SASE is the requirement that the electron trajectory not deviate from the optical axis in order to ensure maximum overlap of the electron and photon beams. A method to monitor the electron beam trajectory inside the undulator is described. Three-dimensional information is obtained by imaging the spontaneous radiation off-axis using pinholes and high resolution position sensors. The expected photon flux properties, the required detector performance, and a conceptual design of the monitor system are given for the free electron laser at the TESLA Test Facility.

1 Introduction

A light source yielding a coherent and bright beam of photons in the VUV to hard X-ray range would provide unique opportunities in many areas of scientific research, ranging from biology to material science [1]. A free electron laser operating in the vacuum ultra-violet (VUV), with tunable first harmonic wavelength in the range of $6\ nm - 70\ nm$ has been proposed at the TESLA Test Facility (TTF) at DESY. During the initial stage, a phase-1 test is planned, with electron beam energy in the range of $300\ MeV$ to $500\ MeV$ [2]. To reach this short wavelength, the self-amplified spontaneous emission (SASE) mechanism is used to generate a high brightness photon beam, with a single passage of a high intensity and brightness electron beam through a long undulator. The interaction of the electron bunch with the intense photon beam generated by its own wiggling motion inside the undulator leads to a density modulation (micro-bunching). Subsequently, the radiation from the micro-bunched beam is coherent and the radiation power increases exponentially until it reaches saturation near the end of the undulator beam line [3, 4].

In order for this self-amplification mechanism to take place, the electron beam must overlap with the photon beam. In our discussion, the photon beam is assumed to be straight. The average electron trajectory, however, can wander away from a straight trajectory. For example, there could be variations in the undulator pole field amplitude or half-period length, which lead to variations in the angular kick imparted to the electron under each

pole. Steering coils are generally used to straighten the electron beam trajectory for an FEL [5]. In order to accomplish this, the electron trajectory, or at least the electron beam positions near the steering stations must be determined. These steering stations are usually placed inside the undulator, at about one gain length apart from each other. The radiated power exponential gain length for TTF-FEL is approximately 1 m. The undulator modules are several meters long. The beam position needs to be determined with precision over this long distance with severe limitation on the space available.

The requirements for a beam position measurement system for the TTF-FEL are listed below:

1. Sensitivity to transverse beam displacement of 10 μm. In general, an overlap of the electron and the photon beams to half the RMS beam width (50 μm at TTF-FEL) is required. In order to obtain at least 90% of the maximum output power, however, the electron trajectory averaged over one gain length should not deviate from the photon beam by more than 10 μm [6].

2. Determination of the beam position with the above sensitivity along the beam line inside the undulator, at locations less than one gain length apart.

3. Compact size: it must fit within a height of 10 mm inside the undulator; or, it must have a length of ≤ 10 cm inside the gap between undulator modules.

4. Ultrahigh vacuum compatibility: parts directly exposed to vacuum may need to be baked because of the clean environment required for superconducting cavities.

5. Must be able to operate in an environment of high radiation flux from beams with 1 nC bunch charge, and high heat load from the FEL beam. An average FEL photon flux up to $10^{23}/m^2/s$ at 28 eV is expected for TTF-FEL phase-1.

6. Bandwidth. It is not necessary to measure the position for each bunch (111 ns spacing, 1 nC charge), although single bunch measurement would avoid any possible beam jitter effects. Information accumulated over many bunches can be used in determining the steering corrections.

In this report, we propose a beam trajectory monitor (BTM) system, in which a single monitor is used to determine the electron bunch position at several points inside a long undulator module. The BTM consists of a set of pinholes and a high resolution silicon position sensor used to image the off-axis spontaneous radiation emitted by electrons traversing the undulator. The method is described in Section 2. The calculation of the properties of the expected spontaneous undulator radiation photon flux at the TTF-FEL is discussed in Section 3. Some features of silicon detectors relevant to the BTM design are reviewed in Section 4. A conceptual design is described in Section 5. A brief discussion on future plans is given in Section 6.

2   Electron Beam Trajectory Imaging

The synchrotron radiation emitted by electrons traversing an undulator can be used to image the electron beam trajectory inside the undulator. For the discussion in this section, the electron bunch is treated as a point source emitting rays of spontaneous radiation. The beam trajectory monitor system described here requires only a single measurement station for each undulator module.

2.1 Method

With the beam trajectory monitor system, three-dimensional information on the beam trajectory is obtained by imaging the spontaneous radiation off-axis using pinholes and high resolution position sensors. The trajectory can be reconstructed using images behind pinholes placed at different azimuthal angles. The basic idea is shown in Figure 1. The method can be illustrated with a simple "simulation". In the simple case of a straight beam trajectory with an overall offset, the resulting trajectory image is a streak on the imaging plane, as shown in Figure 2. In this example, perfect imaging resolution is assumed. The images for rays emitted at every 0.5 m along z and passing through the horizontal and vertical pinholes are shown. For comparison, the case of no beam offsets is also shown. The streak image for an offset beam is at an angle, while that from a centered beam is aligned with the pinhole axis.

The high resolution imaging sensors are placed a distance d behind the pinholes, and are located at several millimeters away from the nominal beam axis. As shown in Figure 1 for the vertical pinhole, the imaging pixels are arranged in two columns in the transverse direction and several rows in the radial direction.[1] In each row, one pixel is located to the left and one to the right of the pinhole (optical) axis. The relative signal in these two pixels is a function of the image position in the transverse direction and is measured with high precision. See Figure 3a. The pinhole size and the sensor pixel size in the radial direction define the "field-of-view". See Figure 3b. Each row of pixels is thus sensitive to the radiation emitted along a segment of the undulator, and images the electron trajectory transverse displacement averaged over the corresponding longitudinal distance.

The BTM also allows definition of an optical axis. If the electron beam trajectory were a straight line on an axis aligned with the pinholes, the images would be two straight lines perpendicular to each other. Any deviation from this condition is detected by the BTM and corrected using steering stations. The resulting straight trajectory defines the optical axis.

2.2 Pinhole optics

Geometrical optics is used in the above discussion. However, the effects of finite pinhole dimensions, and diffraction through the pinholes when imaging VUV radiation must be taken into account. For a high brightness source, photons are emitted into a small phase space area and the point-source approximation can be used. In this case, the diffraction pattern is symmetrical about the photon flux centroid, so that diffraction only broadens the signal distribution but does not affect the image position determination. The additional angular broadening of the image spot due to diffraction is given by $\theta_d = \lambda/w$, where λ is the radiation wavelength and w the pinhole size. For example, for $\lambda = 44\ nm$, $w = 50\ \mu m$, and a distance of 0.5 m between the pinhole and the imaging sensor, the image size would be broadened by 440 μm.

Due to diffraction broadening in the radial direction, the "field-of-view" in the longitudinal direction is larger than that given by simple geometrical ray optics shown in Figure 3b. The pinhole dimension and the pixel size in the *radial* direction are chosen to optimize the resolution along the trajectory. The SASE gain length is approximately 1 m for TTF-FEL, and the betatron phase advance given by the FODO lattice embedded inside the undulator is approximately 180° over each 4.5 m long module. Furthermore, high-pass

---

[1] The radial direction refers to either the x- or y-direction; while the transverse direction is perpendicular to the radial direction.

NOT TO SCALE

Optical axis

A

Electron beam trajectory
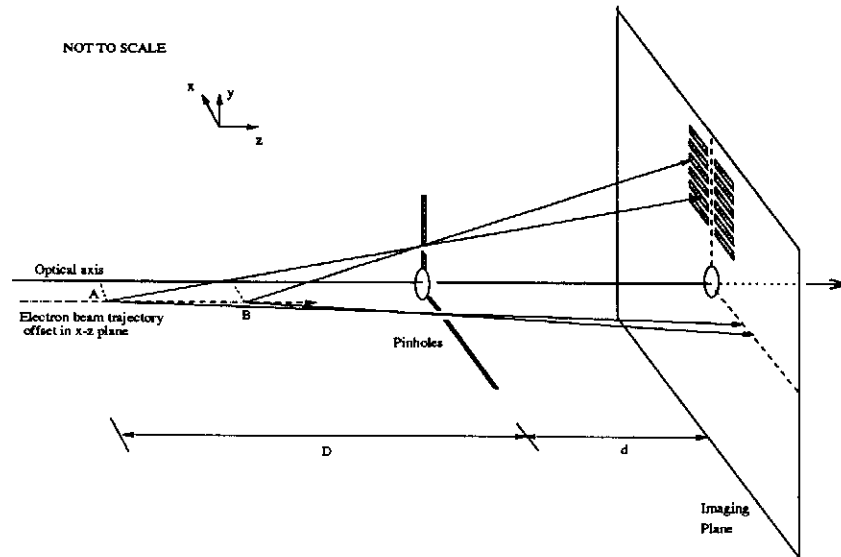offset in x-z plane

B

Pinholes

D

d

Imaging
Plane

Figure 1: The method of the beam trajectory monitor is shown. Pinholes and high resolution position sensors (shown as shaded rectangles behind one of the pinholes) are used to image the synchrotron radiation emitted by the electron and reconstruct the electron beam trajectory.

96/06/28 14.50

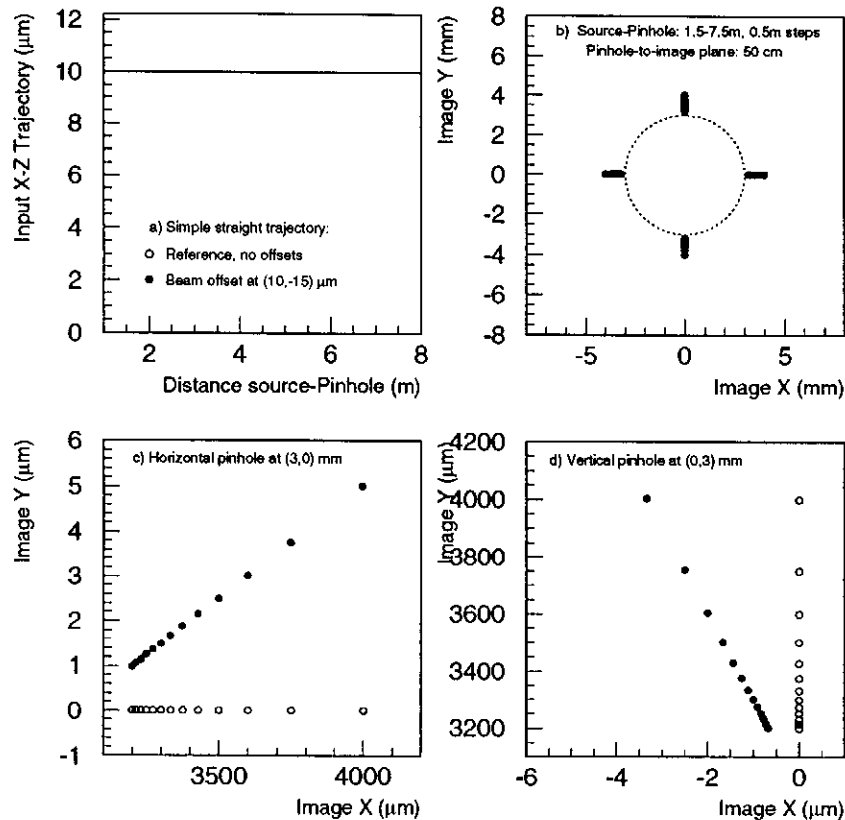## Imaging of Electron Trajectory: Linear

a) Simple straight trajectory:

O Reference, no offsets

• Beam offset at (10,-15) μm

b) Source-Pinhole: 1.5-7.5m, 0.5m steps
Pinhole-to-image plane: 50 cm

c) Horizontal pinhole at (3,0) mm

d) Vertical pinhole at (0,3) mm

Figure 2: Simple simulation of trajectory imaging. a) Trajectory is assumed linear, with 10 μm offset in x and -15 μm offset in y. b) Images behind 4 pinholes in coarse scale. c) Expanded view of the image (solid points) behind a horizontal pinhole for the vertical beam displacement, and d) a vertical pinhole for the horizontal displacement. The reference images of a perfect trajectory are also shown (open points).
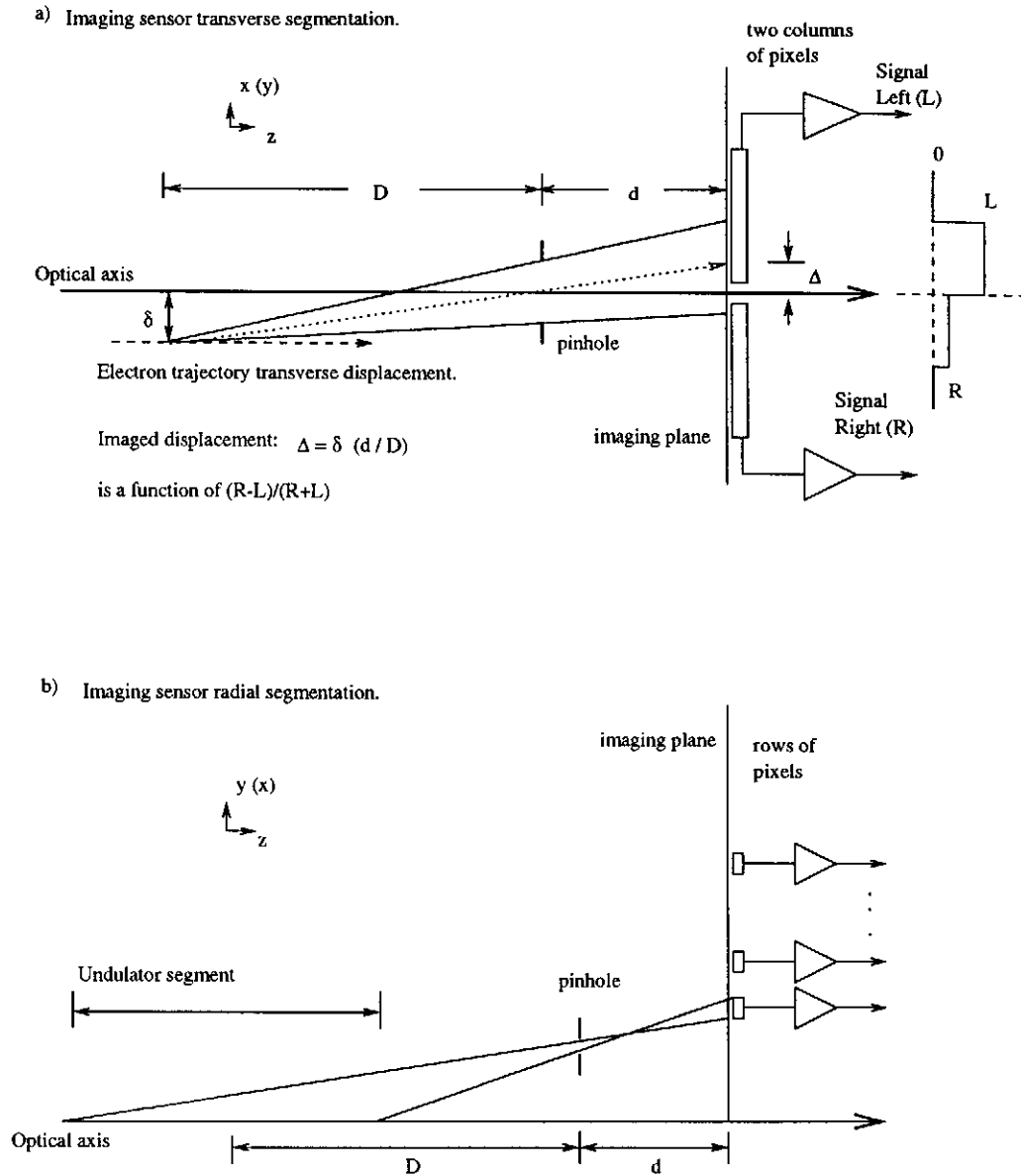
NOT TO SCALE

a) Imaging sensor transverse segmentation.

two columns
of pixels

Signal
Left (L)

x (y)

z

0

L

D

d

Optical axis

Δ

δ

R

Electron trajectory transverse displacement.

pinhole

Signal
Right (R)

Imaged displacement: $\Delta = \delta \ (d / D)$

imaging plane

is a function of (R-L)/(R+L)

b) Imaging sensor radial segmentation.

imaging plane

rows of
pixels

y (x)

z

Undulator segment

pinhole

Optical axis

D

d

Figure 3: Schematic layout of the pinholes and imaging sensors. a) The sensitivity to transverse beam displacement is shown. The imaging sensor is segmented into two columns in the transverse direction. An offset of δ results in a shift in the image by Δ. b) The "field-of-view" over a segment of the undulator is shown. The imaging sensor is segmented into several rows in the radial direction. Photons emitted within this segment are detected by one row of pixels.

Table 1: Pinhole parameters. Distances are measured with respect to the center of the pinhole. Different pinholes are used for the two types of filters.

	500 eV Filter	200 eV Filter
Height (μm)	50	100
Width (μm)	50	50
Thick (μm)	100	100
Distance pinhole-to-first pixel (μm)	50	150
Distance pinhole-to-beam (mm)	3.0	3.0
Distance pinhole-to-sensor (cm)	50.0	50.0

filters at photon energies of 200 eV and 500 eV are used to suppress long wavelength radiations from contributing to image broadening. The additional imaging broadening due to diffraction after filtering at 200 eV (500 eV) is only 60 μm (25 μm) for a pinhole size of 50 μm.

The thickness of the pinhole screen is chosen to minimize the variation in acceptance as the beam displacement changes. This variation is determined from geometrical considerations. For a thickness of 100 μm, the variation is less than 0.1% over a beam displacement range of 500 μm. The image distortion is negligible.

The pinhole width (dimension in the *transverse* direction) affects the photon flux acceptance, the resolution and the sensitivity range to transverse beam displacements. A narrow pinhole subtending a small angular range results in an image whose position is less sensitive to the structure in the illumination pattern. (See discussions in Section 3.3.) It also provides a more sensitive determination of the image position because, for a given image displacement, the change in the left/right signal is larger for a narrower pinhole. An optimal width of 50 μm is chosen. Precision position measurement is available for a beam displacement range of $\pm$ 200 − 250 μm. Outside this range, only the left or the right pixel registers any signal, and this information can be used to bring the beam back into range.

The radial distance between the pixels is chosen to increase the accepted photon flux at large angles, and to minimize the overlap between the imaged trajectory segments. This results in variable radial bin sizes which increase with the radial distance. The pinhole parameters are optimized with the following requirements:

- thickness: sufficient to block VUV radiation without image distortion;

- width: optimal for photon flux and position sensitivity; and

- height: minimal diffraction effects when used together with high-pass filters for optimal longitudinal resolution.

The results are summarized in Table 1.

2.3 Beam trajectory reconstruction

Two imaged space points together with the locations of the corresponding pinholes are sufficient to uniquely determine one space point on the trajectory. When reconstructing

the trajectory, it is à priòri not clear which two points on the image streaks to use because the rates of change along the two images are different when the trajectory (and thus its image) is curved. As is shown below, however, the simple choice of two points at the same radial distance gives good results, and the error resulting from imperfect matches of the two images is only in the longitudinal direction and is small compared to the "field-of-view" length.

The two pinhole positions and the pair of measured image points define two lines which are constrained to the same source point: $\vec{p} = \vec{v} + a \cdot (\vec{u} - \vec{v})$, where $\vec{u}$ and $\vec{v}$ are the image and pinhole locations, respectively, and a is the slope parameter. The result is 6 equations and 5 unknowns ($\vec{p}$ and two slope parameters). Because the two pinholes are at the same distance from the imaging screen, the two slope parameters are identical, and two determinations are available:

$$a_1 = \frac{(h_x - v_x)}{(u_x - w_x) + (h_x - v_x)}, \quad a_2 = \frac{(h_y - v_y)}{(u_y - w_y) + (h_y - v_y)} \tag{1}$$

where $\vec{v}, \vec{u}$ refer to the vertical pinhole and its image, similarly $\vec{h}, \vec{w}$ for the horizontal pinhole. The average is used. The rest of the equations over-constrain $\vec{p}$. Thus, only one well-measured coordinate in the transverse direction from each pinhole image is required. The x-position of the vertical pinhole image and the y-position of the horizontal pinhole image determine the corresponding components of $\vec{p}$.

The reconstruction algorithm described here works for arbitrary beam trajectories. The algorithm is tested using a simple simulation. For the input beam trajectory, sinusoidal oscillations in both the x-z and y-z planes are assumed, with global offsets from the ideal (optical) axis. The input trajectory resembles very roughly the betatron motion in the FODO lattice embedded in the undulator. For each radial bin, with the pinhole parameters of Table 1, the trajectory segment within the "field-of-view" is determined, including effects due to diffraction broadening. The trajectory segment is then scanned in small steps, and at each step, an emitted ray is projected through the pinhole onto the imaging screen. The average transverse position of all the rays in each radial bin is determined. In the radial direction, the bin center is used. The "measured" image points are used as input to the above algorithm to reconstruct the trajectory. The results are shown in Figure 4. The vertical bars result from assuming an image transverse position error of ± 1 μm. The effect of an error in the radial positioning (either due to the pinhole location, or the coarse radial binning) on the order of $5 - 10$ μm is negligible. The imaged trajectory is averaged over a longitudinal distance varying from 0.5 m to 2.5 m as shown by the horizontal bars. Despite the long averaging length, the measured transverse beam displacement is still quite accurate due to the relatively slow variation in the the assumed betatron trajectory. The accuracy improves as the displacement amplitude gets smaller. An iterative correction procedure can be used to obtained a straight trajectory.

2.4 In-situ alignment

Although only two sensors are required, four are used in each BTM station to provide better coverage. One pair of sensors (500 eV filtered) images mainly the small angle (long range) part, while the other pair (200 eV filtered) images the large angle (short range) part of the trajectory. Thus, the sensitive range of each BTM station is longer than the length of one TTF-FEL undulator module. The overlap in the ranges of two consecutive BTM stations allows in-situ alignment. See Figure 4.
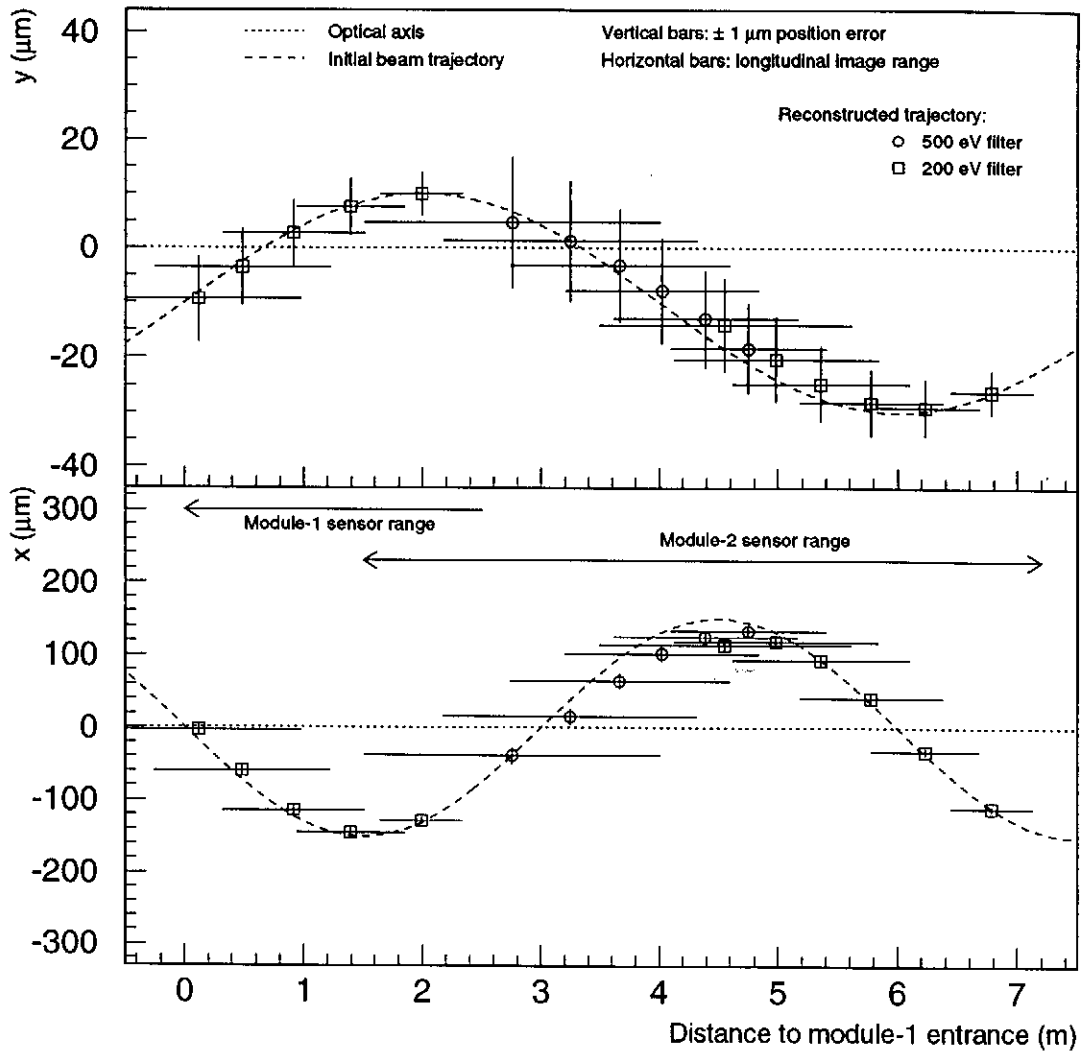
Figure 4: Simulated beam trajectory reconstruction. An arbitrary trajectory is formed with sinusoidal oscillations and offsets in both the x-z and y-z planes. The reconstructed trajectory is shown as points (open circles for the 500 eV filtered detector, open squares for the 200 eV filtered detector). The vertical bars correspond to a ± 1 μm error in transverse image position determination. The trajectory transverse position is averaged over a longitudinal range represented by the horizontal bar.

2.5 Summary

A method to image the electron beam trajectory inside a long undulator module is described. The image position determination and pinhole parameter optimization are also discussed. The trajectory reconstruction algorithm is tested with a simple simulation, and the required beam displacement sensitivity is achieved. The BTM requires only one monitor station for each undulator module, with overlap in the sensor ranges for in-situ alignment. It provides precision beam position information along several points inside the long undulator module. The general method of beam trajectory imaging described above should work with any "diffused" radiation associated with the electron beam motion. As discussed in the next section, the undulator radiation angular distribution is not uniform at all. Nevertheless, over the very small angular range subtended by the pinhole, it can be treated as a "diffused" source.
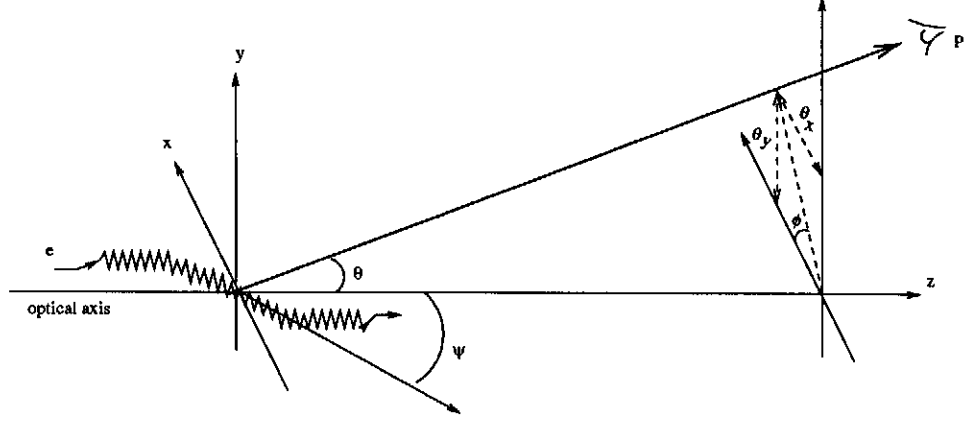
Figure 5: The coordinate system for undulator radiation calculation is shown; θ is the observation angle, and ψ the beam pointing angle.

3 Spontaneous Undulator Radiation

3.1 Basic properties

The general formalism for calculating radiation from an accelerated charge particle is described in [7]. Many discussions on the properties of undulator radiation are available [3, 8, 9]. Some basic results are summarized here. For the TTF-FEL, the planar type undulator is chosen, with the magnetic field alternating in the y direction [2]. The coordinate system is defined in Figure 5. Assuming a perfect sinusoidal undulator field, the electron trajectory obtained by solving the Lorentz force equation is:

$$\vec{r} = (-a\cos(k_u z),\ 0,\ \bar{\beta}_z ct + z_0 \sin(2k_u z)) \tag{2}$$

where $k_u = 2\pi/\lambda_u$; λ_u is the undulator period, and $\bar{\beta}_z c$ the average longitudinal velocity. The angular deflection and the curvature in the x direction are given by

$$\frac{dx}{dz} = k_u a \sin(k_u z), \quad \frac{d^2 x}{dz^2} = k_u^2 a \cos(k_u z), \tag{3}$$

respectively. The radius of curvature corresponding to the field B is given by $\rho = m\gamma c/eB = 1/k_u^2 a$, and the maximum angular excursion $(dx/dz)_{max} = K/\gamma$, where the deflection parameter K is defined by

$$K = \frac{eB}{k_u mc} = 0.934 B[T]\lambda_u[cm]. \tag{4}$$

The amplitude of the trajectory $a = K/k_u\gamma \approx 7\ \mu m$ for the TTF-FEL. In an undulator, K is order of 1 or smaller, and the beam is deflected by approximately $1/\gamma$. The radiation emitted along the undulator can interfere coherently, resulting in a spectrum with sharp harmonic peaks.

Equation 2 also shows that the component of the electron velocity in x varies as $\sin(k_u z)$, while that in z is modulated by $\cos(2k_u z)$. In this simplified picture, the electron motion consists of two harmonic dipole oscillations with the period λ_u along x and $\lambda_u/2$ along z. In the rest frame of the electron, the spontaneous radiation wavelength is the same as the Lorentz contracted undulator period length. For a relativistic electron, the radiation observed in the laboratory frame in the forward direction is Doppler shifted, resulting in

Table 2: TTF-FEL phase-1 parameters for calculation purpose.

Electron beam:	
Energy	380 MeV
Angular divergence	$\sigma_{x'} = \sigma_{y'} = 25 \ \mu rad$
Beam size	$\sigma_x = \sigma_y = 50 \ \mu m$
Bunch charge	$1 \ nC \ (6.4 \times 10^9 \ e)$
Bunch length (σ)	$250 \ \mu m \ (833 \ fs)$
Peak current	480 A
Bunch separation	$111 \ ns$
Number of bunches per train	7200
Repetition rate	10 Hz
Undulator:	
Period	$\lambda_u = 2.73 \ cm$
Magnetic field	$B = 0.497$ T
Deflection parameter	$K = 1.27$

an observed radiation wavelength much shorter than the undulator period. Furthermore, the radiation angle and energy are related. This is described by the expression for the nth harmonic:

$$\lambda_n = \frac{\lambda_u}{2\gamma^2 n}(1 + K^2/2 + \gamma^2\theta^2). \tag{5}$$

So photons radiated at large angles are red-shifted to a lower energy. The fundamental wavelength on-axis for the TTF-FEL phase-1 is 44 nm (or 28 eV in photon energy) assuming 380 MeV beam energy.

3.2 Calculation for the TTF-FEL undulator

For the following calculation of spontaneous undulator radiation spectral and angular properties, the parameters for TTF-FEL phase-1 given in Table 2 are used. The calculation is based on the commonly used computer program URGENT [9]. This program uses the Bessel function approximation in solving the general radiation equation. The far-field approximation is made. (See [10] for discussion on near-field effects.) The undulator magnetic field errors and beam energy spread are not included. The electron beam size and angular divergence is included by convoluting the undulator radiation angular distribution with the electron beam density distribution. The beam is assumed to be Gaussian distributed in x- and y-directions, with widths given by

$$\sigma_u^2 = \sigma_x^2/D^2 + \sigma_{x'}^2, \quad \sigma_v^2 = \sigma_y^2/D^2 + \sigma_{y'}^2 \tag{6}$$

where σ_x and $\sigma_{x'}$ are the RMS beam size and angular divergence in the x-direction, and similarly for y. This approach amounts to a superposition of radiation intensities from the individual electrons, and is valid in the far-field approximation.

The undulator radiation flux in units of photons per second per unit fractional bandwidth

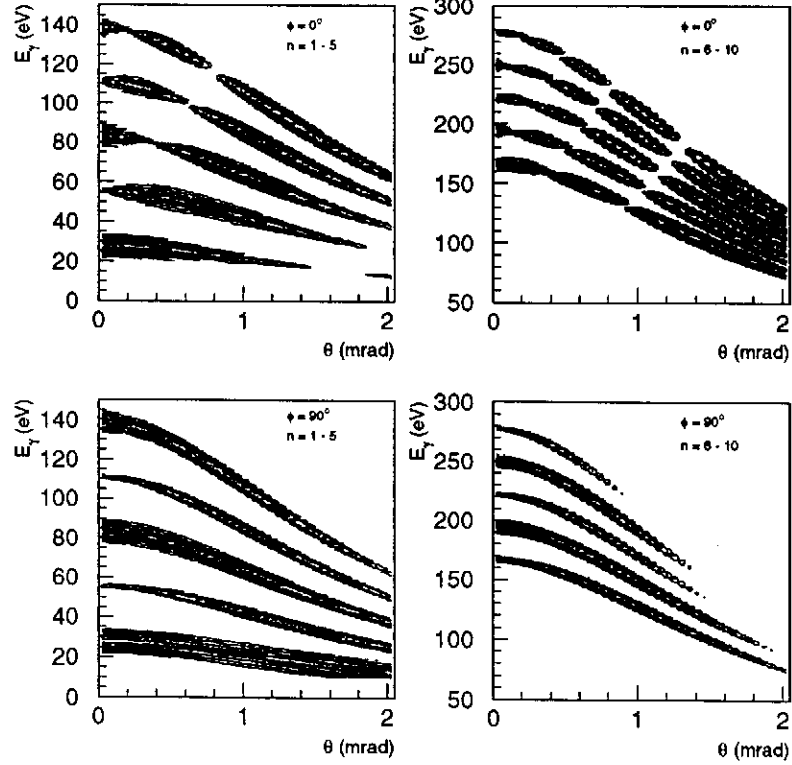**Photon Energy and Angle Correlation**

Figure 6: Contour plot of undulator radiation flux density in the photon energy vs. angle plane. The contour levels represent the flux density in logarithmic scale. The correlation between radiated energy and angle, and the red-shift at large angle are clearly shown here for the first 10 harmonics at two azimuthal angles. An undulator segment of 0.5 m length (or 18 periods) is used in the calculation.

per unit solid angle is given by

$$\frac{d^2 I}{d\Omega(d\omega/\omega)} = 4.55 \times 10^{16} \gamma^2 N_u^2 I_b \sum_{n=1}^{\infty} F_n(\theta, \phi) \cdot L_n(\Delta\omega/\omega_1), \tag{7}$$

where N_u is the number of undulator periods traversed and I_b the beam current. The angular properties for the nth harmonic is described by $F_n(\theta, \phi)$, while the frequency dependence at a given angle is given by the sinc function:

$$L_n(\Delta\omega/\omega_1) = \frac{\sin^2(N_u\pi\Delta\omega/\omega_1)}{(N_u\pi\Delta\omega/\omega_1)^2}, \quad \Delta\omega = \omega - \omega_n, \quad \omega_n = 2\pi c/\lambda_n. \tag{8}$$

More details on the calculation of $F_n(\theta, \phi)$ can be found in [8, 9] and are summarized in Appendix A. To ascertain proper use of the program, the calculated photon flux frequency spectrum for the ALS undulator U8.0 with $K = 0.9$, $\lambda_u = 8$ cm, and beam energy at 1.52 GeV is compared with those measured [12]. The total flux, estimated by the product of the peak and FWHM of the spectrum for harmonics 1, 3 and 5, agrees to better than 25%. This gives an estimate on the accuracy of the present flux calculation.

The correlation between the photon angle and energy for the TTF-FEL phase-1 is shown in Figure 6 for several harmonics. It is clear that any selection criteria on photon energy would also affect the observed angular distribution. The photon flux energy spectrum is
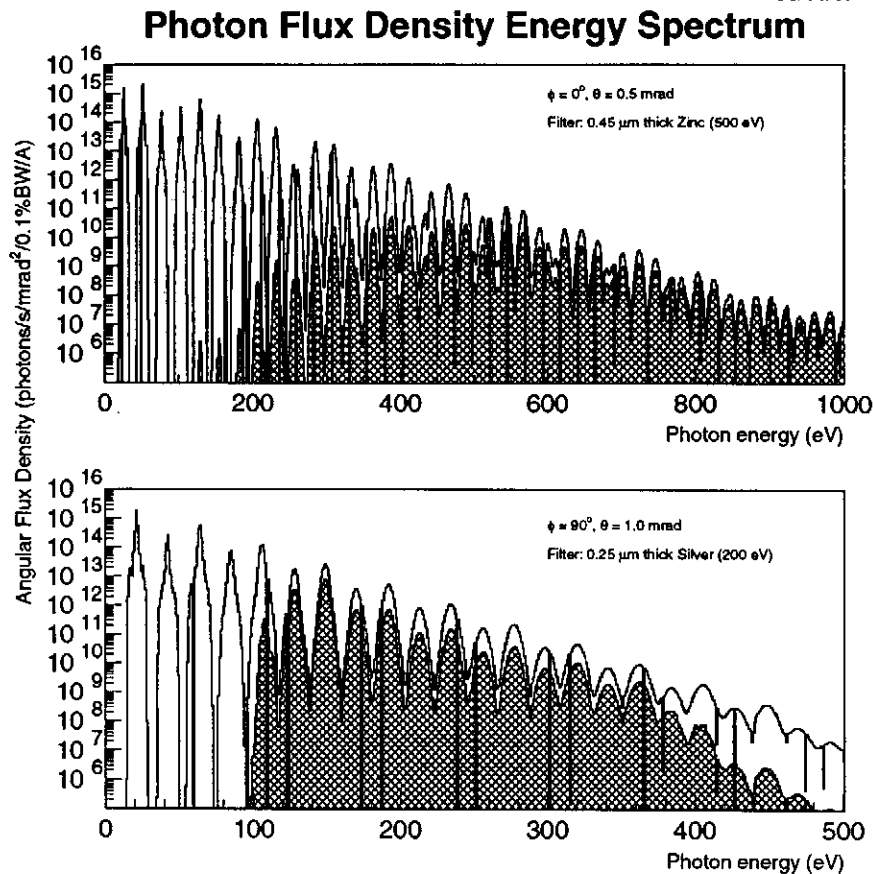
Figure 7: Undulator radiation flux density energy spectrum at two angular positions. The shaded plots show effects of the high-pass filters. Note the logarithmic scale - approximately 10 orders of magnitude suppression of the lower harmonics is achieved with the filters. An undulator segment of 0.5 m length (or 18 periods) is used in the calculation.

shown in Figure 7. As discussed in Section 2.2, high-pass filters are used to suppress long wavelength radiations in order to reduce diffraction broadening. The effect of applying the high-pass filters is also shown. The enormous flux in the lower harmonics is clearly suppressed as desired. The filter transmission is calculated using measured optical constants [13].

3.3 Photon flux angular distribution

For the purpose of beam trajectory imaging, it is important to know the undulator radiation illumination pattern at the pinhole. As the electron beam propagates through the undulator, its pointing angle changes due to kicks by misaligned quadrupoles and magnetic field errors, as well as betatron motion. It is important that the resulting jitter in the illumination pattern does not lead to an apparent beam trajectory displacement in the BTM.

The peak power density $(Watts/mrad^2)$ angular distributions, calculated for harmonics 1 to 50 are shown in Figure 8 in the angular range $0 - 1.5$ $mrad$ in 40 μrad steps, for several individual harmonics, as well as the sum of those harmonics with a central energy above 200 eV at any given angular position. Only a quadrant of the full distribution is shown. It is worth pointing out the following features:

1. The flux distribution is not azimuthally symmetric, although it is left-right and up-down symmetric.

96/11/19 15.16
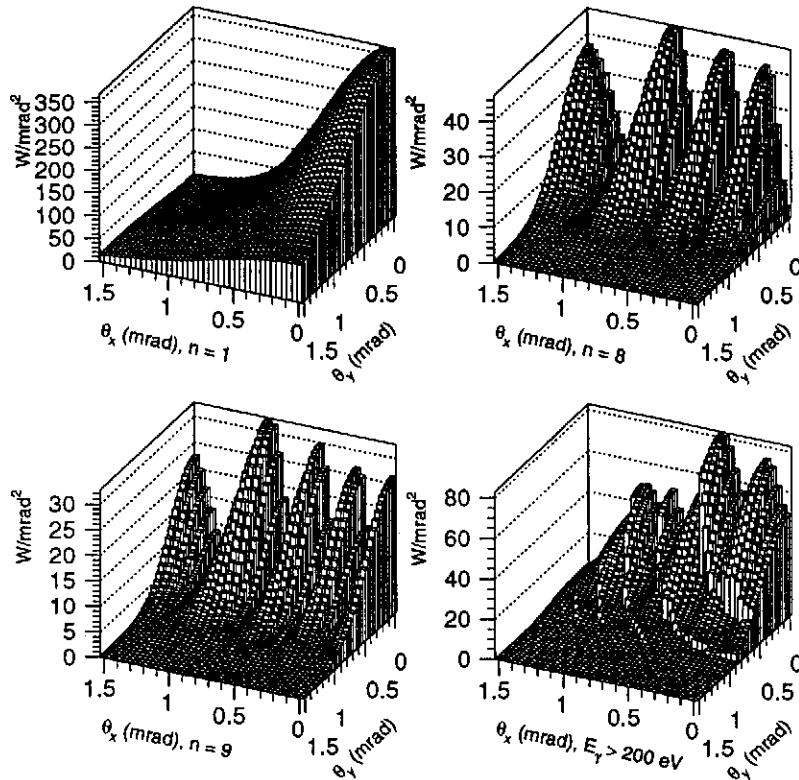
UR Power Density Angular Distribution, 380 MeV

Figure 8: Undulator radiation peak power density angular distribution for $\theta_{x(y)}$ up to 1.5 mrad. Individual harmonics 1, 8, and 9 are shown. The superposition of harmonics with energy above 200 eV at the plotted angular position is also shown.

2. There are n peaks for the nth harmonic.

3. There is no on-axis radiation for the even harmonics.

4. The flux is still reasonably large even at a relatively large angle of 1 mrad.

5. The requirement on E_γ to be above a threshold leads to a cut-off on $\theta = \sqrt{\theta_x^2 + \theta_y^2}$ for a given harmonic, because of the correlation between photon energy and angle.

The angular range subtended by the pinhole is typically 10 μrad, much smaller than the angular range shown in Figure 8. Furthermore, the filter transmission and the detection efficiency dependence on the photon energy also need to be included. The calculation is repeated for the range of ± 400 μrad centered at the pinhole position in 4 μrad steps . The results are shown in Figure 9 for the vertical pinhole.

The distribution is fairly smooth, aside from some stepped structure. To estimate the image position error due to structures in the illumination pattern, the beam angle is varied by ± 360 μrad for several beam displacements. The radiated power is extrapolated to the left and right sensor pixels (see Figure 3a), and the position error with respect to the ideal image position is calculated. The error is much less than 1 μm. The position error due to a "step" in an otherwise uniform distribution is given by $\epsilon = \alpha w/4$ in the worse case when the step occurs in the center of the image, where w is the pinhole width,

96/11/19 18.39
Power Density Angular Distribution

θ_x (mrad), 200 eV filter * detection efficiency

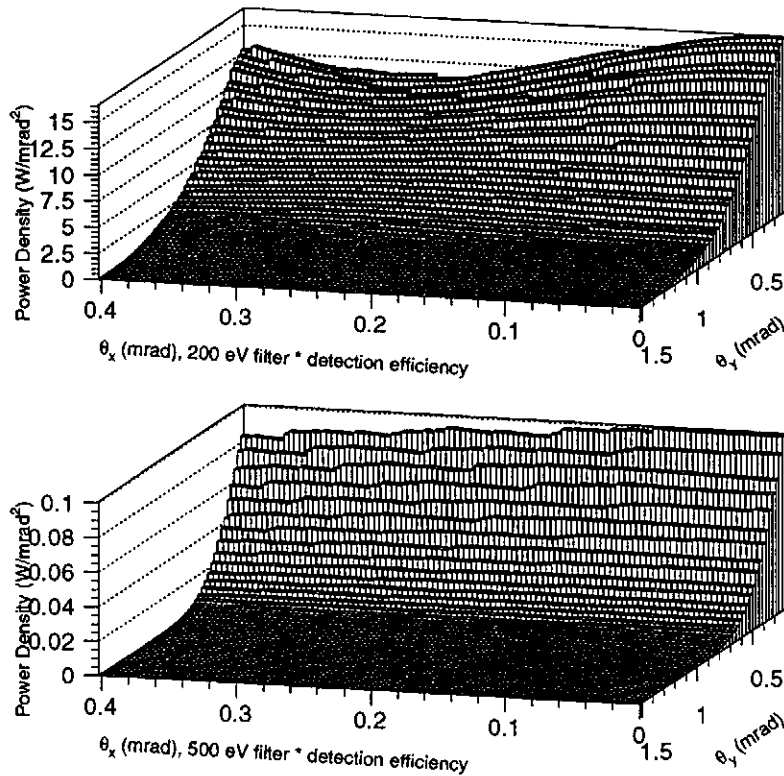θ_x (mrad), 500 eV filter * detection efficiency

Figure 9: Undulator radiation peak power density angular distribution. Illumination pattern at the vertical pinhole (on y-axis) is shown. Effects from detection efficiency and filter transmission dependence on photon energy are included. The range in θ_x shown is 400 μrad, while the pinhole typically subtends an angular range of 10 μrad.

α the fractional difference between the signal to the left and the right of the step. So, for $\epsilon < 1~\mu m$ and $w = 50~\mu m$, α must be $< 8\%$. This condition is satisfied here, and may be taken as a criteria for a "diffused" light source in the context of beam trajectory imaging.

3.4 Signal and sensitivity estimates

As described in Section 2, the imaging detector is segmented in the radial direction. The signal expected in each pixel bin is estimated, using the signal power density angular distributions shown in Figure 9. The θ position of each radial pixel bin is given by the bin center and the center of the undulator segment within its "field-of-view", including broadening due to diffraction. The variation in the angular acceptance of the pinhole as the source point moves along the undulator is taken into account. The filter transmission and VUV detection efficiency are included. The electron-hole pair creation energy in silicon is assumed to be 4 eV at this photon energy.

The results are summarized in Table 3. The radial segmentation and the corresponding coverage along the undulator are given. The angles θ_1 and θ_2 are given by the radial bin center and the beginning and end, respectively, of the undulator segment within the "field-of-view". Finally, the expected signal in number of electron-hole pairs in each radial bin is given for the two types of filters. Two pairs of horizontal and vertical pinholes

14

Table 3: The radial imaging binning, the corresponding range along the undulator and the angles subtended, and the expected photon signal (in electron-hole pairs) for a single bunch are shown. Both radial and longitudinal distances are measured with respect to the pinhole. The signal is calculated including the filter transmission and VUV detection efficiencies. The bunch charge is assumed to be 1 nC. Only a subset of all possible radial bins is shown here, and is used in the trajectory reconstruction simulation shown in Figure 4.

Radial bins (μm)		Long. Range (m)			θ_1	θ_2	Signal (e)	
Center	Width	Center	Min.	Max.	$(mrad)$	$(mrad)$	0°	90°
500 eV filter								
277.	20.	6.0	5.0	7.5	0.544	0.547	0.58E+03	0.96E+02
297.	20.	5.6	4.7	6.8	0.590	0.594	0.46E+03	0.52E+02
317.	20.	5.2	4.4	6.3	0.638	0.642	0.38E+03	0.34E+02
337.	20.	4.9	4.2	5.8	0.686	0.690	0.31E+03	0.18E+02
362.	30.	4.5	3.8	5.4	0.745	0.752	0.29E+03	0.11E+02
392.	30.	4.1	3.6	4.9	0.819	0.826	0.22E+03	0.49E+01
200 eV filter								
403.	20.	4.3	3.5	5.6	0.786	0.791	0.20E+06	0.51E+05
443.	20.	3.9	3.2	4.9	0.886	0.891	0.12E+06	0.26E+05
488.	30.	3.5	2.9	4.4	0.998	1.007	0.75E+05	0.14E+05
553.	40.	3.0	2.5	3.7	1.166	1.179	0.57E+05	0.46E+04
648.	50.	2.5	2.2	3.1	1.422	1.441	0.55E+05	0.52E+03
823.	100.	2.0	1.7	2.4	1.914	1.964	0.22E+05	0.42E+01

and detectors are planned. One pair would be equipped with a 200 eV filter and the other with a 500 eV filter. For $\theta < 1$ $mrad$, the signal flux passing through both filters are sufficient. But because of diffraction broadening, the longitudinal resolution for the 200 eV filtered detector would be much too large, and the 500 eV filtered detector is used. For $\theta > 1$ $mrad$, the signal flux for the 500 eV filtered detector becomes too small, and the 200 eV filtered detector is used. The signal expected in each imaging bin is shown as a function of the bin radial position in Figures 10a and b. Comparing with Table 3, the first 6 bins are used for the 500 eV filtered detector; while every other bin is used for the 200 eV filtered case. The signal is the weakest at $\phi = 90°$ for large angles, as small as 5 e. Therefore, for some of the imaging bins, the signal would need to be accumulated over order of 100 bunches (≈ 10 μs). Also, for the 200 eV filtered detector, the expected signal variation range is several orders of magnitude. These should be kept in mind when considering the readout electronics noise and dynamic range.

The sensitivity to electron beam transverse displacement should be better than 10 μm. An estimate of the sensitivity to beam displacement can be obtained from simple geometrical considerations, as illustrated in Figure 3a. As shown in Figure 10c, the sensitivity to a finite beam transverse displacement is the worst for the point furthest from the imaging screen because of the reduced lever-arm. Figure 10d shows that for a 10 μm beam displacement sensitivity, a 1 μm position resolution is required, although for points close to the BTM a larger position resolution is acceptable due to the increased imaging lever-arm. Note that
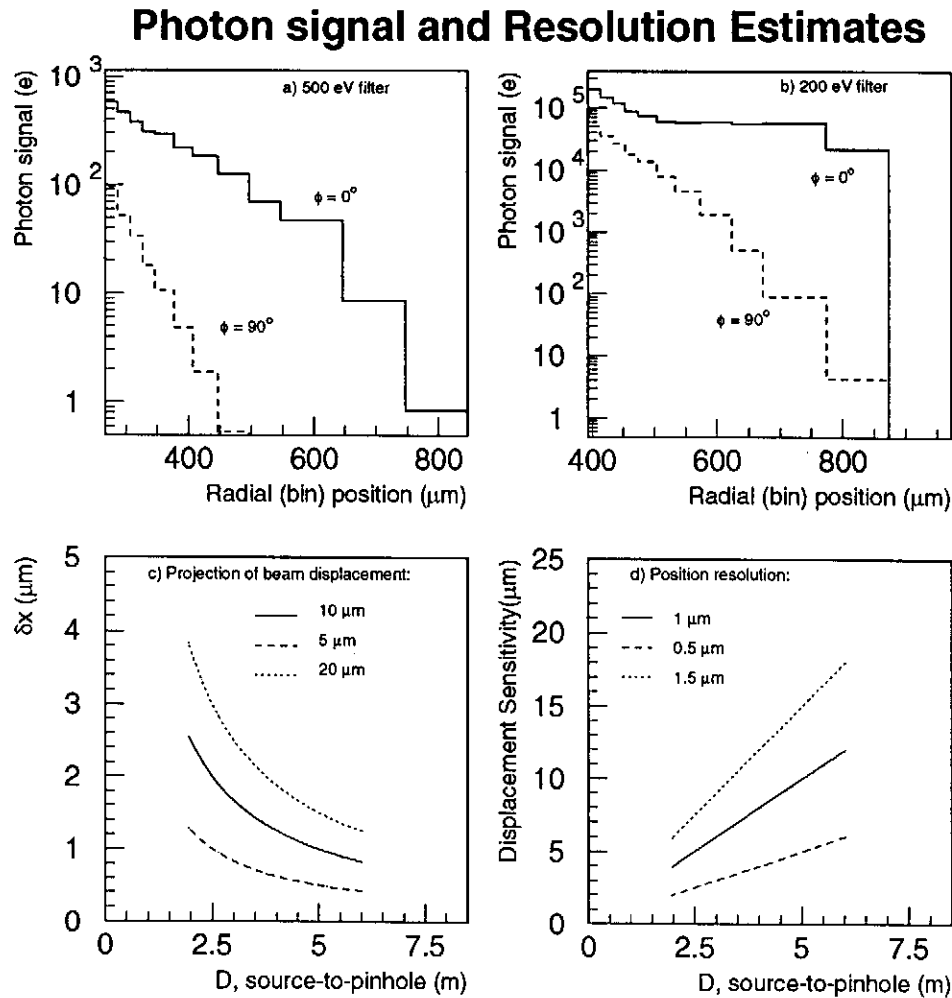
Photon signal and Resolution Estimates

Figure 10: The photon signal in electron-hole pairs in each radial imaging bin is shown as a function of bin position for $\phi = 0°$ and $\phi = 90°$, for a) 500 eV filtered detector and b)200 eV filtered detector. The required position resolution for various beam displacements is shown in c); while the beam displacement sensitivity for various position resolutions is shown in d) as a function of the distance of the radiation source to the pinhole.

the steering coil can be used to induce a well defined beam movement to test the imaging system resolution.

In the case of TTF-FEL phase-2, the beam energy would be 1 GeV. The central radiation cone would be narrower, but the photon energy would also be extended to a higher range. Similar calculations for phase-2 show similar results as for phase-1, and the conclusions of the above studies should also apply.

3.5 Summary

The properties of spontaneous undulator radiation for the TTF-FEL phase-1 setup have been studied in detail. The photon flux at relatively large emission angles remains significant, making it feasible to place a beam trajectory monitor several millimeters from the beam line. Calculations for the phase-2 beam energy of 1 GeV show similar results.

4 High Resolution Position Sensors

Due to the compact size and high precision requirements, silicon detectors are considered for the position sensors. The techniques of position determination at the micro-meter level for charge particles and X-rays using silicon detectors have been developed over the last decade, for applications in high energy physics experiments, astrophysics, and biological sciences. A number of excellent papers on silicon detectors [14, 15] exists where further details can be found. In this section some issues relevant to the BTM imaging sensor design are reviewed. The detection of VUV radiation is described first, followed by a discussion on position resolution and noise in silicon detectors and associated readout electronics.

4.1 Response of silicon detectors to VUV radiation

In an X-ray silicon detector, the energy of the incident photon is absorbed and distributed to photo- and Auger- electrons, which then transfer kinetic energy to the crystal lattice by phonon scattering. As long as this energy transfer is larger than the band gap, which is 1.12 eV in silicon, electrons in the valence band can be freed. The result is electron-hole pair creation. The primary electrons can also give rise to secondaries, resulting in a cascade of pair creation. Under the influence of an applied potential, the electron-hole pairs separate, and the charge cloud drifts toward a collection anode.

Not all of the absorbed photon energy goes into freeing valence electrons; a fraction of it turns into lattice vibrations. The energy required to create one electron-hole pair (w) is observed to depend on temperature and the photon energy. At room temperature, experimental data show that on average $w = 3.64\ eV$ at $E_\gamma = 1400\ eV$ and w increases slowly for smaller E_γ, by 8% at $E_\gamma = 300\ eV$ [16]. We use the value $w = 4\ eV$ for signal estimation. The number of photons absorbed per unit length at a given depth of z is given by the attenuation law: $dN/dz = -N_0/\lambda_a(E_\gamma) \cdot exp[-z/\lambda_a(E_\gamma)]$, where the attenuation length $\lambda_a(E_\gamma)$ is dependent on the photon energy and the material. The attenuation lengths for silicon and several common doping materials are plotted against photon energy in Figure 11a. The X-ray absorption data compiled in [13] are used. There is a very strong absorption for photons between $100\ eV - 500\ eV$. It is therefore important that the layer of entrance window material be very thin, less than a few $100\ nm$, in order to reach high detection efficiency in VUV.

Lechner and Strüder in [16] describe a model of ionization signal generation in X-ray silicon detectors, which contains essentially two processes: the absorption of the photon energy which creates electron-hole pairs, and the collection of the ionization charges. Their detector has a back-entrance window containing a thin p^+n diode (Boron doped) and no passivation layer. The charge cloud is assumed to be a sphere of uniform density. A charge collection efficiency function is used to describe the probability that an electron generated at the depth z will reach the collection anode. It divides the detector into three regions: next to the detector surface on the entrance side is a dead-layer where the electron-hole pairs created are not separated by an internal field; then comes a region where some of the charges are lost due to recombination or trapping; and finally a region closest to the collection anode where all charges are collected.

This model is used in [16] to fit the measured photon energy spectrum, and extract the detection efficiency defined as the ratio of the average measured photon energy and the incident photon energy. The measurement was made for $E_\gamma > 350\ eV$, and it showed good agreement with the detection efficiency obtained differently for a photo-diode fabricated with the same process. The photo-diode efficiency was measured by normalizing

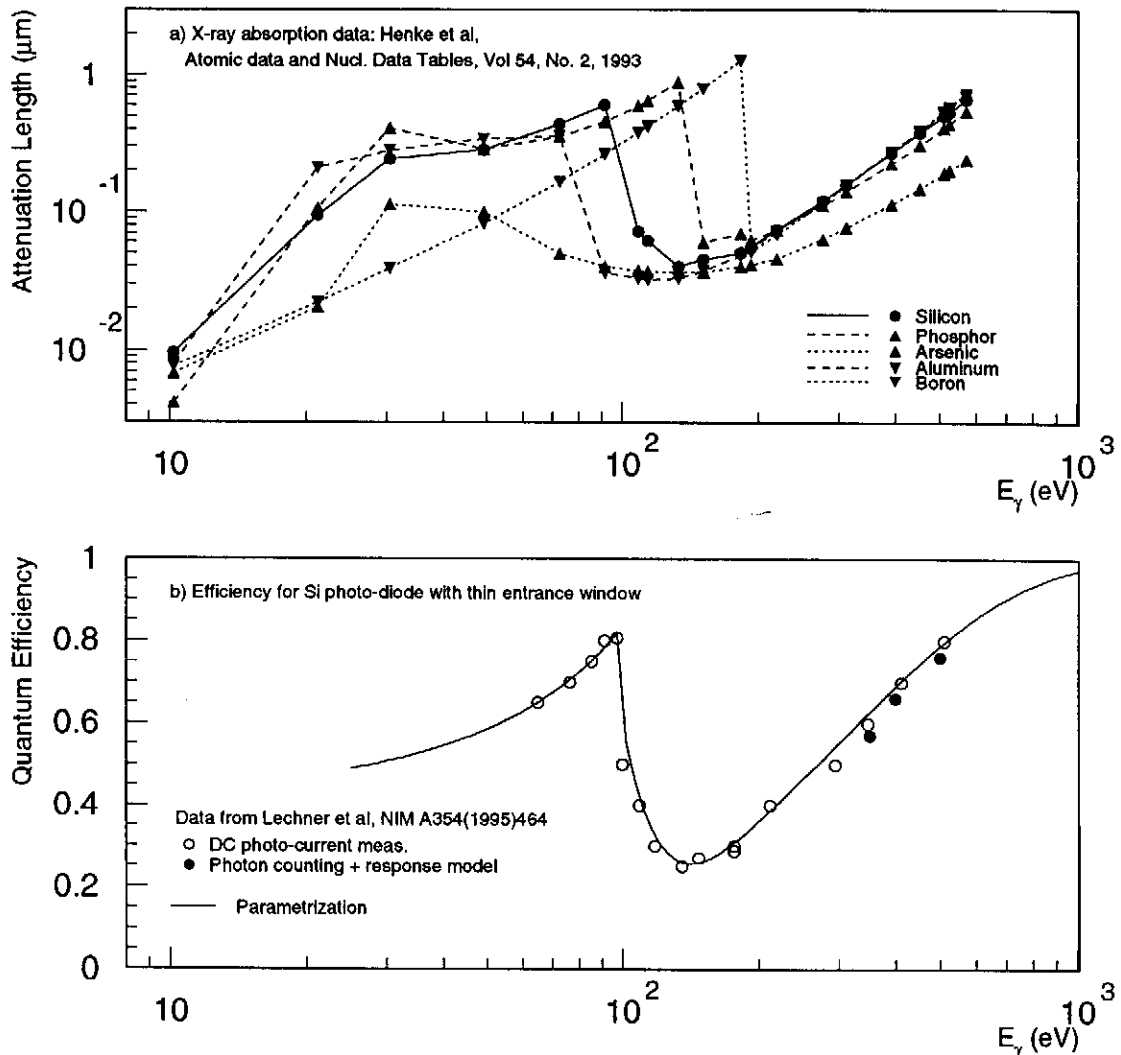# Absorption And Detection Efficiency in VUV

Figure 11: a) Attenuation length for VUV radiation in silicon, as well as several doping material commonly used in silicon detectors. b) Photon detection efficiencies for silicon detectors fabricated with an ultra-thin back-entrance window.

its response to a constant flux of mono-energetic photons to that of a reference diode with known efficiency, and then multiplying by the reference efficiency. This photo-diode efficiency measured down to 65 eV is shown in Figure 11b along with the results obtained from the response model (based on Figure 9 of [16]). The energy dependence of the detection efficiency follows closely that in the attenuation length for silicon, indicating a very thin dead layer and very high charge collection efficiency. The detection efficiency is the lowest at 20% just above the absorption edge at 100 eV, and rises to 80% at 500 eV.

4.2 Position resolution and noise considerations

The position resolution of silicon detectors is determined by the signal-to-noise ratio. The signal collected at the anode depends on the range of the primary and secondary particles, and the drift field used in charge transport (that is, the doping uniformity and the sensor pattern definition). The noise is given by the readout electronics (amplifier capacitance and

series resistors) and the detector parameters (leakage currents and capacitance). It also depends on the measurement time. The electronics can be designed to optimize the signal-to-noise ratio for a given readout bandwidth. In strip-type detectors, because the charge cloud diffuses during transport, charge sharing among the strips can be used to obtain a position resolution better than that given by the strip pitch. In a silicon drift chamber, the charge cloud is guided towards small readout anodes in a well defined narrow channel by appropriately biasing the silicon wafer [17]. The drift time then determines the position in one direction, while the anodes can be segmented orthogonal to the drift direction providing two-dimensional position measurement. Discussions on position determination using silicon drift chambers can be found in [17, 18]. However, a timing resolution of $0.1\ ns$ would be required for a $1\ \mu m$ position resolution. And the large spread in the signal spot size could lead to signal loss.

In the following, position determination from charge interpolation is considered in detail, and estimates of the achievable position resolution are given. A fully depleted detector with a thin, unpassivated back-entrance window similar to that described in Section 4.1 is assumed. The expected photon flux described in Section 3.4 is used.

4.2.1 Position determination by charge interpolation

For silicon detectors with segmented micro-strips or pixels, a non-linear charge interpolation algorithm can be used to obtain a position resolution better than the expected $\Delta/\sqrt{12}$ where Δ is the distance between the strips [19]. Let η be a non-linear transformation of the incident particle position x, $\eta = \eta(x)$. (In the case of imaging a flux of photons with a finite spot size, x corresponds to the average image position.) Conservation of probability leads to $|p(\eta) \cdot d\eta| = |p(x) \cdot dx|$. The η distribution is determined mainly by the shape of the charge distribution $f(x)$. Assuming a uniform distribution in x, and using the η distribution measured in the data sample, the particle position can be determined for each event

$$x = \Delta \int_{\eta_{min}}^{\eta} p(\eta')d\eta' - X_0, \tag{9}$$

where X_0 is a constant relating the origins of the x and η scales.

For estimates of position resolution, a detector configuration shown schematically in Figure 3a is assumed. The signal charge distribution $f(x)$ is assumed to be either Gaussian or uniform, and η is defined as

$$\eta(x) = \frac{R(x) - L(x)}{R(x) + L(x)}, \tag{10}$$

where

$$R(x) = N \int_{-x}^{\infty} f(x')dx' \quad \text{and} \quad L(x) = N \int_{-\infty}^{-x} f(x')dx' \tag{11}$$

are the number of electron-hole pairs measured in the right and left pixels, respectively.[2] The function $f(x)$ is normalized: $\int_{-\infty}^{\infty} f(x) \cdot dx = 1$, and N is the total number of e-h pairs generated by the incident flux of undulator radiation in this row of two pixels. From this definition we also obtain $\frac{d\eta}{dx} = 2f(-x)$, so that the error on x is $\delta x = \frac{\delta\eta}{2f(-x)}$. The error on η is

$$\delta\eta = \frac{1}{2}(1 - \eta^2)\sqrt{(\frac{\delta R}{R})^2 + (\frac{\delta L}{L})^2} \tag{12}$$

---

[2]The variable η is sometimes defined as $R/(R + L)$. The final results are of course the same.
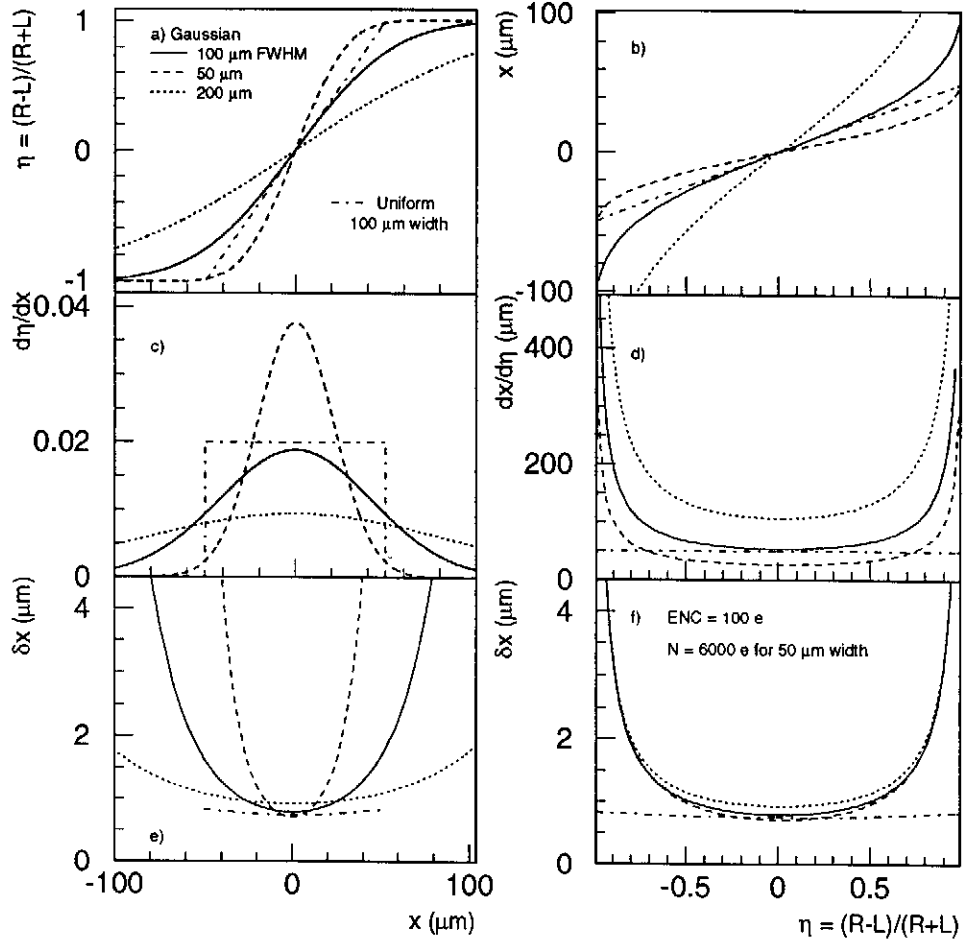
Figure 12: Position determination by charge interpolation. The charge distribution is assumed to be either Gaussian or uniform, with various widths. The position resolution assuming a noise of 100 e and a signal of 6000 e is given in e) and f). In the left column, various quantities are plotted as a function of the image position (related to the beam transverse displacement); while in the right column, they are plotted against the relative signal in the right and the left pixel.

where the error on the measured signal charge is due to the statistical error and the equivalent noise charge (ENC), $\delta R = \sqrt{R + ENC^2}$ and similarly for δL. Both the signal charge and the noise charge are measured in number of electrons. The capacitive coupling between the left and the right pixels is small and the correlation between δR and δL is ignored. A significant capacitive coupling between neighboring pixels would lead to an increase in the total noise charge.

The relations between η, $\frac{d\eta}{dx}$ and x are shown in Figures 12a - d. As discussed in Section 3.3, within the small angular range subtended by the pinhole, the undulator radiation angular distribution is approximately uniform in the transverse direction. This uniform distribution would be smeared out symmetrically by a sinc function due to diffraction through the pinhole. For the following estimates, a uniform and a Gaussian distributions are considered, with FWHM ranging from 50 μm to 200 μm. The position resolution is shown as a function of x and η in Figure 12e and f, respectively, for a signal of 6000 e and a

noise of $ENC = 100$ e. For a Gaussian charge distribution, the resolution is seen to be the best when the image position is near the center, and degrades slightly off the center. The case of the smaller width has a slightly better resolution at the center, but also has the larger non-uniformity. The best result is obtained for a uniform charge distribution. The resolution dependence on the pinhole width is small, because the contributions from statistical error and the gradient $\frac{dx}{d\eta}$ balance each other. But as discussed in Section 3.3, a smaller pinhole width minimizes sensitivity to structures in the illumination pattern.

4.2.2 Noise and capacitance specifications

For a given photon flux signal, the required position resolution is to be achieved by minimizing the noise. Low-noise signal processing has been discussed in detail by Radeka [20]. Some results are summarized here. The amount of noise is determined by the characteristics of the detector and the amplifying device, the operation temperature, the impulse response of the signal processing filter, and the signal measurement time. In the following, room temperature operation and a filter with triangular impulse response are assumed. The sources of noise in charge amplifiers can be represented by the following equivalent noise generators at the input:

1. Series white noise (ENC_s). It is the intrinsic transistor noise appearing as fluctuations in the current through the conduction channel during the charge amplification process. This is the thermal noise in the conducting channel for FET, and the shot noise of charge carriers being randomly injected from the emitter into the base for bipolar devices. It can be represented as a voltage generated by the thermal noise of an equivalent resistance in series with the input. For bipolar devices, the base resistance must be included. $ENC_s \propto (C_D + C_A)t_m^{-1/2}$, where C_D is the detector capacitance, C_A the amplifier gate-to-channel junction capacitance (gate-to-source for FET, base-to-emitter for bipolar), and t_m the measurement time over which charge is accumulated.

2. Parallel white noise (ENC_p). It is due to noise currents flowing into the detector sensing electrode, such as shot noise from detector leakage currents or input transistor base current, as well as thermal noise of dissipative elements connected to the input. It can be represented as a current source and a resistor in parallel to the detector capacitance. $ENC_p \propto t_m^{1/2}$ and is independent of the total capacitance.

3. Series $1/f$ noise ($ENC_{1/f}$). It is due to fluctuations in charge in the gate to conduction channel interface. It appears as an equivalent voltage generator in series with the gate, and has a power spectrum frequency dependence of approximately $1/f$. $ENC_{1/f} \propto (C_D + C_A)$ but is independent of t_m. It is very small for FET and bipolar devices, but several orders of magnitude higher for MOS devices.

4. Noise in dielectrics (ENC_d). It is due to thermal fluctuations in dissipative components such as fiber glass circuit boards and frequency dependent resistors. ENC_d appears as a $1/f$ noise current source in parallel to the input, and is independent of the total capacitance and t_m.

For short measurement times, the noise is dominated by ENC_s. It decreases with increasing t_m ($ENC_s \propto t_m^{-1/2}$) to a minimum $ENC \approx 10$ e set by the $1/f$ noise when t_m is in the range of $10 - 100$ μs. For longer measurement time, the ENC rises again because of the parallel noise ($ENC_p \propto t_m^{1/2}$). For a given set of detector and amplifier parameters,

the series noise charge can be estimated by [20]:

$$ENC_s[e] = 0.79 \times 10^3 \sqrt{a_n \, C_D[pF]} \left[\sqrt{\frac{C_D}{C_A}} + \sqrt{\frac{C_A}{C_D}} \right] \sqrt{\frac{\tau_A}{t_m}}, \qquad (13)$$

where τ_A is the device time constant approximately equal to the electron transit time through the conduction channel and $a_n \approx 2/3$ for FET and $1/2$ for bipolar devices. For example, for the pn-CCD with integrated on-chip JFET amplifier with $C_D \approx 0.030 \, pF$ and $C_A \approx 0.09 \, pF$ [21], ENC_s is estimated to be 11.6 e for $t_m = 250 \, ns$ and a typical device time constant $\tau_A = 0.5 \, ns$. This is to be compared with the measured noise of 11.1 e at room temperature using an ^{55}Fe source [22].

For a single 1 nC bunch in the TTF-FEL, the expected signal as summarized in Section 3.4 and Table 3 is very weak for some radial bins for the 500 eV filtered detector at $\phi = 90°$, ranging from only 5 e at $\theta \approx 0.8 \, mrad$ to 100 e at $\theta \approx 0.5 \, mrad$. In order to image the full beam trajectory as shown in Figure 4, the signal must be accumulated over approximately 100 bunches ($t_m \approx 10 \, \mu s$). As shown in Figure 10c, typically an 1 μm resolution is needed to resolve a 10 μm beam displacement; while at large θ (or short distance), the corresponding position resolution required is 2 μm because of the larger lever arm. The image position resolution is shown as a function of the image position for several assumed signal and noise values in Figure 13. The weak expected signal leads to a tight tolerance on noise, resulting in a limit of $ENC < 20 \, e$ in order to achieve the required position resolution. Assuming a matched capacitance ($C_D \approx C_A$) and $\tau_A = 0.5 \, ns$, the corresponding limit on capacitance is $C_D < 4.7 \, pF$ for $t_m = 10 \, \mu s$. For a matched capacitance of $C_D = C_A = 1 \, pF$, which is not a very stringent requirement for small pixels, the corresponding noise is $ENC_s \approx 9 \, e$. The pixel area is approximately 250 $\mu m \times 20 \, \mu m$. As a comparison, the anode area of the pn-CCD is approximately 90 $\mu m \times 16 \, \mu m$, and its capacitance of 0.03 pF is dominated by the capacitance to nearby guard rings.

4.3 Summary

Some salient features of silicon detectors relevant for high resolution position measurement have been described. The method of position determination by charge interpolation is discussed, and the expected resolution given in terms of signal and noise. It is robust and the implementation is straightforward. The noise specification can be met with existing technology, and the required resolution can be achieved.

As a diagnostics device, it is desirable to provide a fast output signal which is directly proportional to the beam displacement. Some methods for directly encoding position information in electronic circuits can be found in [23].

5 Beam Trajectory Monitor Conceptual Design

In the previous sections, the basic idea of beam trajectory imaging and the major ingredients for its realization are discussed. In this section, a conceptual design of the BTM is given. A schematic layout of the BTM with respect to the undulator, the vacuum chamber, and the beam line is shown in Figure 14. In the following, each component of the BTM system is described in detail. For the sake of discussion, the BTM detector assembly is assumed to be located in the gap between the undulator modules, with the pinhole assembly installed inside the beam pipe upstream of the detector. The compatibility of this layout with the TTF-FEL is discussed below.

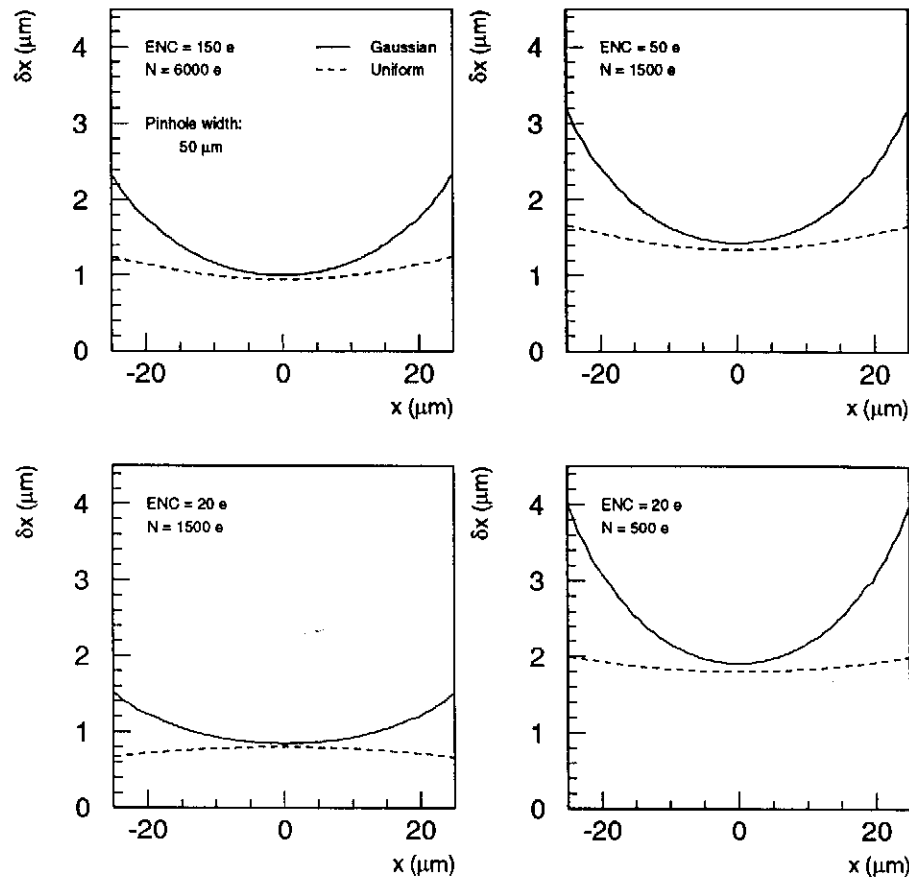**Position Resolution and Signal-to-Noise**

Figure 13: Position resolution as a function of image position for various signal and noise assumptions. The initial signal charge distribution is assumed to be either Gaussian (solid) or uniform (dashed). A signal of $N = 1500$ e ($N = 500$ e) is the worst case for which a 1 μm (2 μm) resolution is required in order to determine the beam displacement with a 10 μm resolution, with an accumulation over 100 bunches each of 1 nC charge.

5.1 Detector assembly

The detector assembly consists of a position sensor, a high-pass filter, and a veto counter all enclosed in a RF shield for protection against electromagnetic fields excited by the beam. A schematic layout is shown in Figure 15.

5.1.1 Silicon detectors

Silicon detectors are chosen because of the limited available space and the required position resolution. The silicon bulk should be fully depleted. The back-entrance window must be very thin in order to be efficient for VUV radiation above 200 eV. As shown schematically in Figures 3 and 16, the position sensor consists of two columns of pixels, arranged in rows in the radial direction. The pixel dimensions are approximately 250 μm × 20 μm. The beam displacement sensitive range is determined by the active area of the position sensor. A sensor active range of ±200 μm in the transverse direction would provide a coverage of ±2 mm beam displacement at a distance of 5 m upstream. Even though precise position determination is available only for a range of ±250 μm beam displacement, the beam "in/out" information can be used to center the beam. A 0.5 mm range in the radial direction would allow the beam trajectory to be imaged, up to 2 m in front of the pinhole
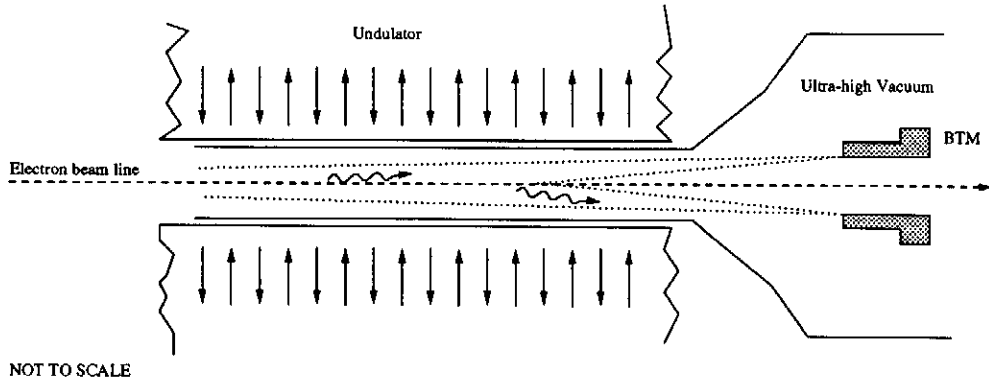
NOT TO SCALE

Figure 14: A schematic layout showing the beam trajectory monitor, the undulator, and the electron beam line. The BTM is located inside ultra-high vacuum. The dotted lines indicate the sensitive range.

(see Table 3). So the position sensor should have an active area of at least $0.5\ mm \times 0.5\ mm$. The thickness of the silicon wafer is approximately $300\ \mu m$. The VUV photon signal flux is completely absorbed within this thickness. This can be used to separate the signal from backgrounds due to penetrating particles, such as stray electrons in the beam halo or scattered hard X-rays. A veto counter PIN diode placed behind the position sensor can be used to reject measurements dominated by background. If the background rates turn out to be high, a second position sensor can be used instead, and the background signal in each pixel subtracted.

5.1.2 RF shield and high-pass filters

The RF shield should protect the detector and the front-end electronics from electromagnetic fields propagating in the beam pipe. The (lower) cutoff frequency of a cylindrical wave guide is given by

$$\nu_{c,pipe}[Hz] = \frac{1}{2\pi}\frac{2.405\,c}{b},$$ (14)

where b is the beam pipe radius. The skin-depth is given in MKS units by

$$\delta = \sqrt{\frac{\rho}{\pi\mu\nu}},$$ (15)

where ρ is the resistivity, μ the permeability, and ν the frequency. The attenuation of the field penetrating into the shield is proportional to $e^{-\delta \cdot z}$, where z is the penetration depth. For $b = 5\ mm$, $\nu_c = 23\ GHz$, the skin-depth for copper ($\rho = 1.678 \times 10^{-8}\ \Omega\,m$) is $\delta = 0.43\ \mu m$. So a copper shield approximately $1\ mm$ thick is more than sufficient.

A cut-out in the RF shield is needed to let the VUV undulator radiation pass through onto the detector. This VUV window has an area given by the position sensor active area. The high-pass filter, made of a thin layer of conductive material ($0.25\ \mu m$ silver or $0.5\ \mu m$ zinc), covers the VUV window and is electrically connected to the RF shield. It can be coated onto the back entrance window of the position sensor but should be electrically isolated from it. For RF fields with wavelength comparable to the copper shield thickness, the cut-out behaves like a wave guide and RF fields with frequency below cutoff are shielded.
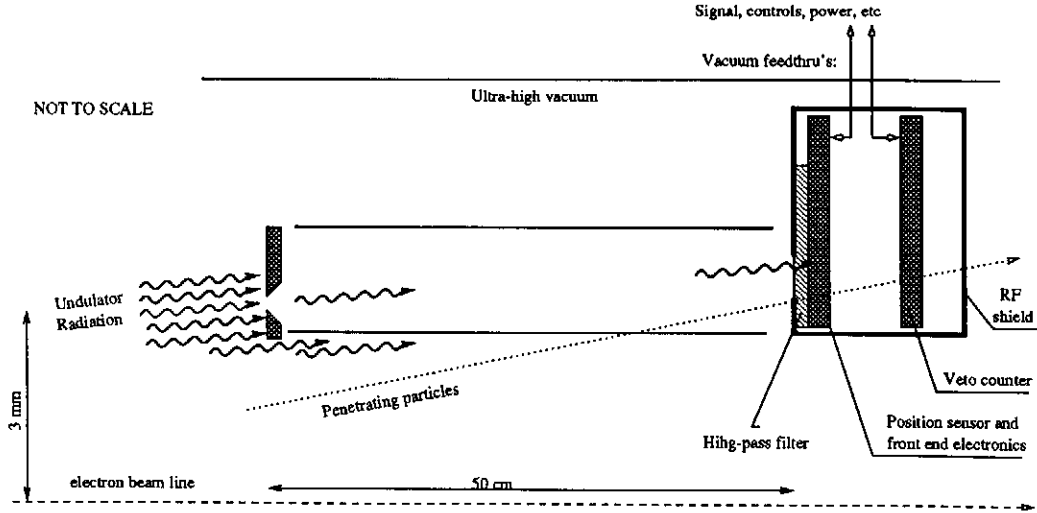
Figure 15: Layout of the detector and pinhole assembly. The side view of one pinhole-detector is shown. There are in total four pinhole-detectors, placed symmetrically around the electron beam line.

For a rectangular waveguide, the cutoff frequency is given by

$$\nu_{c,rect}[Hz] = \frac{1}{2\pi}\frac{\pi c}{a},\tag{16}$$

where a is the larger of the cross-sectional width and height. In this case, $a = 0.5\ mm$, and $\nu_c = 300\ GHz$. The corresponding wavelength $\lambda_c = 1\ mm$ is comparable to the thickness of the copper shield. The RF fields with frequency above this cutoff would come through the VUV window, but they are strongly attenuated by the high-pass filter material. For silver $(\rho = 1.586 \times 10^{-8}\ \Omega\,m)$, $\delta \approx 0.12\ \mu m$, and for zinc $(\rho = 5.916 \times 10^{-8}\ \Omega\,m)$, $\delta \approx 0.22\ \mu m$ at $\nu = 300\ GHz$. These depths are approximately a factor of 2 smaller than the corresponding filter thickness. The frequency spectrum of electromagnetic fields excited by the short bunch extends up to 190 GHz, corresponding to a bunch length of 250 μm. Beyond that, the field intensity falls off rapidly. The VUV window dimension and the filter thickness or material can be further optimized with respect to RF shielding and VUV efficiency. Detailed knowledge of the RF fields intensity and frequency spectrum are required.

5.1.3   Front-end electronics

A schematic layout of the front-end electronics for the silicon detector readout is shown in Figure 16. Because the expected signal is very small $(1000\ e = 0.16\ fC)$, the amplifiers must be located near the detector. Each pixel is connected to an amplifier channel via a bonding wire a few millimeters long, so the front-end electronics are located inside the vacuum chamber.

Each readout channel consists of a charge-sensitive amplifier [20, 24]. A reset switch across the feedback capacitor is used to discharge the accumulated signal, and the readout channel is ready for the next measurement. Filtering is achieved by multiple sampling, and integration on the storage capacitor. There are 12 channels per position sensor for a total of 48 channels, and 4 veto detector channels. The analog signals are sent out serially via the buffer/multiplexer. This front-end architecture is similar to those found in high
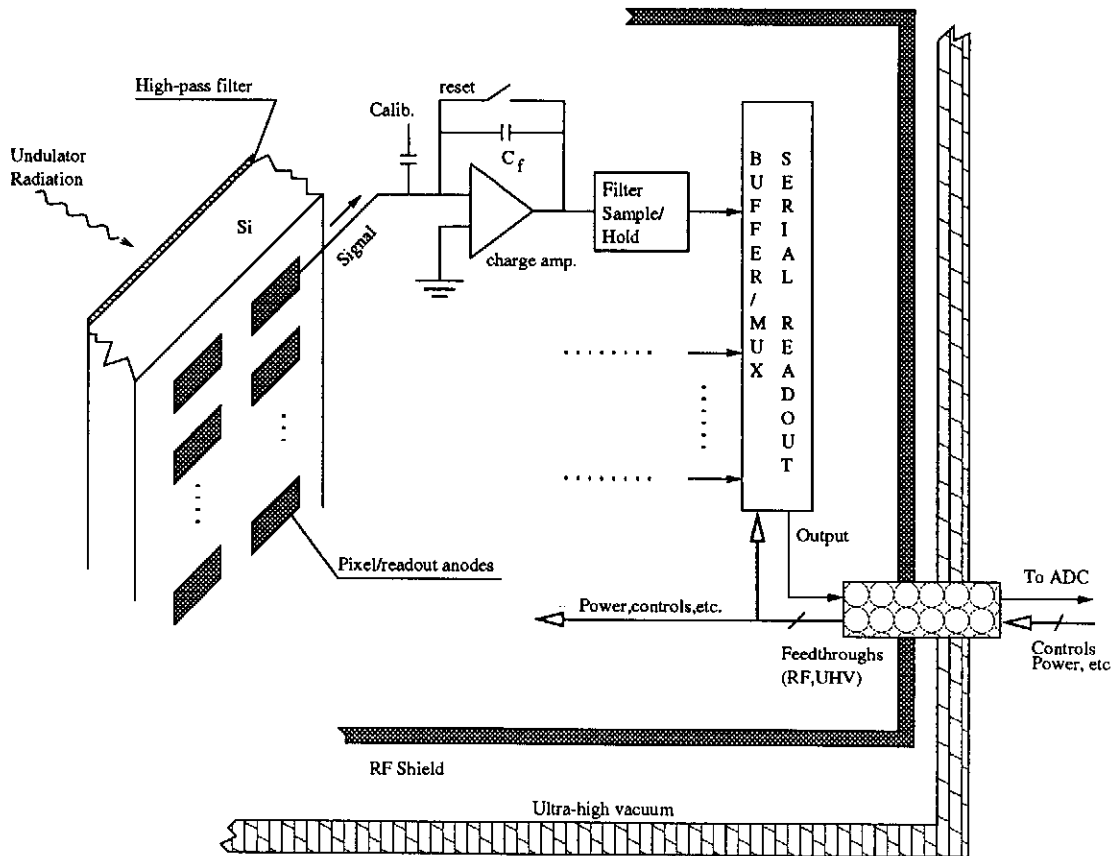
Figure 16: Schematic layout of the front-end electronics. It is located next to the detector, and enclosed in an RF-shield, all inside ultra-high vacuum.

energy physics experiments now running or planned for the future. The total number of control signals and power lines to the front-end chips is approximately 30. Feedthroughs with more than 30 isolated conductors, compatible with UHV are available commercially. These are needed to send out the signal, and receive the power lines and control lines.

As discussed in section 4.2.2, the measurement time should be optimized for low-noise signal processing. It should also have a large adjustable range around the value $t_m \approx 10\ \mu s$, which can be accomplished by remotely controlling the reset switch, while maintaining low noise performance. This feature is important, in case the signal size changes, due to variation in bunch charge or other factors. The total capacitance should be $< 1\ pC$, and the noise $ENC < 20\ e$ at room temperature. If necessary, the first JFET amplifier can be integrated onto the detector wafer as done for the pn-CCD [21].

The multiplexed output is sent to an ADC, and then via VME network to host computers for trajectory reconstruction. For quick turn-around diagnostics, a branch of the output can be sent to fast position encoding circuits to provide online position information. The front-end electronic components should be relatively radiation-hard, as they are placed near the beam.

5.1.4 Calibration and monitor

The readout electronics can be calibrated and monitored with precision test charge injections. It is essential to maintain the calibrations between the left and the right pixels. A

pulsed light-emitting diode can be used to monitor the status of the position sensor, and also check the calibration of the readout electronics.

5.1.5 Radiation damage

The detector assembly is located at 3 mm away from the nominal beam line (Figure 15). For the design TTF-FEL beam parameters, the electron and FEL beams have a RMS width of 50 μm, and a Gaussian density distribution. The number of beam electrons and FEL photons at a radius of 3 mm is negligible. Most of the spontaneous radiation flux is at low energy, as shown in Figure 7, and does not have enough kinetic energy to cause bulk damage. The silicon sensor should not have an oxide passivation layer, in order to avoid the problem of trapped surface charges which would lead to increased leakage current. Using the silicon heat capacity and assuming 2×10^4 photons at 100 eV are absorbed within an attenuation length of 0.1 μm and an area of 10 $\mu m \times 20$ μm, the increase in bulk temperature is estimated to be much less than 1 degree. Thus, radiation damage from the electron beam and heat loading from the FEL beam is expected to be negligible.

The radiation from backgrounds, such as dark currents from field emission in the accelerator cavity or hard X-rays from bremstrahlung has not been considered. Detailed estimates of the expected fluxes are not yet available.

5.2 Data acquisition and user interface

The front-end signals are sent to ADCs located in an VME crate. The digitization granularity should not contribute significantly to the position error. The signal range is approximately 2 orders of magnitude (Table 3). The commonly available 12-bit ADC can accommodate this range, as well as a factor of 10 variation in the bunch charge. The digitized information is processed by DSP modules and the data sent via network to a remote computer for detailed analysis and storage. The front-end clock and control signals are generated in a VME module. The calibration and monitoring of the front-end electronics are done remotely via computer control.

5.3 Mechanics

The RF shield for the detector assembly also serves as mechanical support. The space taken up in the undulator module gap is < 10 cm. The whole assembly can be retracted, to avoid accidental radiation damage, and to reduce beam impedance.

5.3.1 Pinhole assembly

As discussed in Section 2.2, the pinhole should be approximately 50 μm high, 50 μm wide and 100 μm thick. Precision laser-drilled pinholes made of stainless steel or copper several tens of microns thick can be made, as for standard optical pinholes available commercially. The mechanical support for the pinholes should be made of non-conductive material, to reduce beam impedance. It is located 0.5 m upstream of the detector assembly, inside the beam pipe. In addition, a long cylindrical shell concentric with the beam pipe is needed to block the radiations passing "under" the pinhole.

5.3.2 Alignment

The detector and the pinhole assembly should be retractable. Since the transverse pinhole position defines the optical axis, precision stepping motors and linear translation assembly

should be used. The BTM's at two consecutive modules can be aligned in-situ, since there is an overlap of the trajectory imaged. This is shown in Figure 4. With trajectory imaging averaged over many measurements, a relative alignment of the BTM stations with a precision of a few microns can be expected. The absolute placement should be reproducible within the range of the undulator magnetic center, with a relaxed tolerance of several 10's of micro-meters.

It is also possible to use semi-transparent silicon strip sensors together with a reference laser line to align the BTM's over a distance of $5 - 20$ m to order of 2 μm accuracy [25]. In this case, the transparent sensors are mounted on each BTM, and the laser reference is brought in at the beginning of the undulator beam line.

5.3.3 Infrastructure

For the front-end electronics located inside the vacuum chamber, the heat generated should be small and is carried away by thermal conduction. For the DAQ electronics, VME crate power and cooling are required. Twisted-pair shielded cables are needed for data and control signals. Stable power supplies are needed for biasing of the electronics and the silicon detectors. In case the laser alignment system is desired, optical tables, and supports for mirrors and collimators at the beginning and end of the undulator line are also needed.

5.4 Compatibility with the TTF-FEL

5.4.1 Wakefield considerations.

Electromagnetic fields are excited as the electron bunch (or its induced wall current) crosses a discontinuity. This wakefield could act back on the beam and lead to a degradation in the beam qualities. The longitudinal component of the wakefield leads to a non-uniform energy loss along the bunch length, and some of the loss by particles in the front part of the bunch could be transferred to those in the tail, resulting in an increased energy spread. The transverse component leads to a change in the transverse momentum along the bunch, an angular deflection which produces transverse emittance growth.

The presence of the BTM leads to discontinuities in the vacuum chamber. After the electron trajectory has been fine-tuned, the BTM system is in principle no longer necessary. It can therefore be retracted away from the beam to minimize beam impedance. There are also various schemes to minimize wakefield effects due to discontinuities in the vacuum chamber [26]. Detailed numerical calculations of the wakefield effects are being carried out for various structures.

5.4.2 Ultra-high vacuum

The BTM system must be compatible with ultra-high vacuum (UHV). Material containing chemical compounds of hydrogen and carbon ($H_X C_Y$), hydrogen and fluoride ($H_X F_Y$), CO, or CO_2 are not allowed. The pinhole assembly, the mechanical support, and the RF shield are made of material that can be baked. Care must be taken to minimize out-gassing from the detector assembly and the readout electronics.

5.4.3 Discussion

For the present design, the ideal location for the BTM would be in the gap between the undulator modules, which would allow imaging of the electron beam trajectory through the complete undulator beam line. However, the mechanics of a vacuum chamber with a

Table 4: Summary of the conceptual layout of the beam trajectory monitor.

Detector:

active area	$> 0.5\ mm \times 0.5\ mm$;
resolution	$\leq 1\ \mu m$ (transverse), $5 - 10\ \mu m$ (radial);
entrance window	dead-layer $< 50\ nm$;
efficiency	$> 80\%$ at $E_\gamma = 500\ eV$;
operation temp.	300 K;
location	a minimum distance detector-to-beam of 3 mm;

Pinhole:

dimension	50 μm high, 50 μm wide, and 100 μm thick;
location	3 mm from beam, 50 cm from position sensor;

Readout/DAQ:

readout rate	10-50 μs measurement time;
noise	total capacitance $< 1\ pC$, $ENC < 20\ e$ at room temp.;
calibration	charge injection and LED;
ADC	12-bit digitization;

Mechanics:

UHV	compatibility with ultra-high vacuum;
RF shield	copper shield plus conductive filter material;
other	precision linear translator assembly.

10 mm magnetic gap is already quite challenging, and the installation of the BTM pinhole assembly inside the beam pipe would further complicate the design. As a first test of the BTM concept, it is suggested that a single BTM be placed at the end of the undulator beam line. It would allow us to learn to use this method of beam trajectory determination in a realistic environment, and to study the background conditions and wakefield effects without affecting the FEL operation.

5.5 Summary

A practical layout of the BTM is described. The system parameters are summarized in Table 4. Some open questions such as wakefield effects and dark current backgrounds need to be addressed by further detailed studies. The BTM concept nevertheless appears feasible for the TTF-FEL.

6 Future Plans

6.1 Proposal for a prototype test

In order to validate the BTM concept, the undulator radiation properties described in Section 3 must be verified, and the high resolution position sensor must be demonstrated. As discussed in Section 4, the technologies for making high resolution silicon position sensors for VUV radiation, as well as low-noise signal processing electronics are available.

It is nevertheless important to demonstrate that the required sub-micron resolution can be achieved. The aim is to construct a prototype, and carry out the following laboratory tests using various light sources (LEDs, X-ray tubes, and possibly undulator/wiggler) to verify the BTM concept at least in an ideal environment.

1. Detector performance.

   - Position resolution - measurement using a focused light source, together with a linear translation stage with sub-micron step size.

   - Efficiency for VUV radiation - measurement at an existing undulator/wiggler light source, using monochromatized light. The photo-current is measured, and compared with respect to calibrated reference diode fabricated in the same way as done in [16].

   - Background rejection - measure the response to minimum ionizing particles using a Ru^{106} source, and measure the response to hard X-rays using light sources.

   - Trajectory reconstruction - simulate radiation along a trajectory with several precisely located flash lamps, and reconstruct their positions from the images taken simultaneously.

2. Readout electronics.

   - Readout speed - the light source is pulsed and the frequency is varied to confirm low-noise operation for a range of measurement time.

   - Position encoding - performance of the fast position encoding circuit is tested using a light source as above.

In addition, it may be necessary to carry out characterizations of the silicon detector with respect to depletion, doping profile, capacitance and noise performance to understand the test results. Detailed systematic studies of the readout electronics performance may also be required.

With a working prototype, a test at an existing undulator beam line would be extremely valuable to ensure that the complex radiation pattern in fact does not affect the beam trajectory imaging method. And finally, tests in an UHV environment can be made to ensure out-gassing is not a problem.

6.2 Division of responsibilities

In order to proceed to a technical realization, the major responsibilities for the BTM system need to be identified, and distributed among the participating groups.

1. Mechanics - design and construction of a) the RF shield and detector assembly support structure, b) the pinhole assembly support structure, and c) interfaces to the vacuum chamber, and precision motorized linear translators. The mechanical support should be designed to have minimal beam impedance.

2. Detector and readout - design, construction, and test of a) a sub-micron resolution silicon detector for VUV radiation with the capability to separate VUV from penetrating radiations; b) low-noise front-end electronics with precision charge calibration at the level of < 1%; and c) a light calibration system for monitoring of the detector and front-end electronics.

3. Data acquisition and user interface - design and implementation of a) position encoding circuit for fast turn-around monitoring; b) VME hardware and software for readout and control of the front-end electronics, LED calibration pulser, and interface to remote computer; c) hardware and software, and interface for fast automatic steering correction; and d) software for detailed data analysis and graphics display in the control room.

4. Infrastructure - responsibility for a) cabling for electronics readout, control, and calibration; b) power supplies; and c) cooling water.

7 Conclusions

We have described the beam trajectory monitor (BTM) which can be used to determine the electron trajectory inside a long undulator module. Studies presented in this report show that it is feasible to build such a system for the TTF-FEL. Diagnostics of the electron beam trajectory are important for the successful operation of the SASE FEL proposed for the TESLA Test Facility. The same method, however, can be applied at any planned 4th generation light sources using long undulator modules. The plan is to build a prototype and verify the BTM design concept.

Acknowledgement

A Undulator radiation angular distribution

The angular properties of undulator radiation are described by $F_n(\theta, \phi)$ in Equation 7 of Section 3.2:

$$
\begin{aligned}
F_n(\theta, \phi) &= |\vec{A}_n(\theta, \phi)|^2, \\
\vec{A}_n &= \xi(2\gamma\theta\cos\phi\, S_1 - K\frac{2nS_1 + 4S_2}{X}, \quad 2\gamma\theta\sin\phi\, S_1, \quad 0).
\end{aligned}
\tag{17}
$$

The intensity of radiation along the polarization direction $\hat{u}$ is proportional to $|\vec{A}_n \cdot \hat{u}|^2$, where $\hat{u} = (1, 0, 0)$ for the linear component along x, for example. S_1 and S_2 each contains an infinite sum of Bessel functions:

$$
S_1 = \sum_{p=-\infty}^{\infty} J_p(Y)J_{2p+n}(X), \quad S_2 = \sum_{p=-\infty}^{\infty} pJ_p(Y)J_{2p+n}(X),
\tag{18}
$$

where

$$
X = 2\xi\gamma\theta K\cos\phi, \quad Y = \xi K^2/4, \quad \xi = \frac{n}{1 + K^2/2 + \gamma^2\theta^2}.
$$

When $\theta = 0°$ or $\phi = 90°$, $X = 0$ and Equation 17 cannot be used directly. The Bessel function recurrence relation $J_{\mu+1}(x) + J_{\mu-1}(x) = 2\mu J_\mu(x)/x$, and the properties $J_\mu(0) = \delta_{\mu 0}$ and $J_{-\mu}(x) = (-1)^\mu J_\mu(x)$ are used to obtain

$$
S_3 \equiv \frac{2nS_1 + 4S_2}{X} = \sum_{p=-\infty}^{\infty} J_p(Y)[J_{2p+n+1}(X) + J_{2p+n-1}(X)].
\tag{19}
$$

So that at $X = 0$, S_1 and S_3 simplifies to

$$S_1 = \sum_{p=-\infty}^{\infty} J_p(Y)\delta_{2p+n,0}, \quad S_3 = \sum_{p=-\infty}^{\infty} J_p(Y)(\delta_{0,2p+n+1} + \delta_{0,2p+n-1}),$$

and that

- for n even: $S_1 = J_{\frac{n}{2}}(Y)$, $S_3 = 0$;
- for n odd: $S_1 = 0$, $S_3 = J_{-\frac{n+1}{2}}(Y) + J_{-\frac{n-1}{2}}(Y)$.

The Bessel functions $J_\mu(x)$ are calculated using upward recurrence relations for any x and μ starting from $J_0(x)$ and $J_1(x)$. The infinite sum is truncated, using the property that $J_\mu(x)$ decreases monotonically for $\mu \gg x$. Calculations are done numerically [11].

References

[1] Workshop on Scientific Applications of Coherent X-rays, J. Arthur, G. Materlik, and H. Winick (editors), SLAC Report 437, 1994; Workshop on Fourth Generation Light Source, M. Cornacchia and H. Winick (editors), SSRL Report 92/02, 1992.

[2] TTF-FEL Conceptual Design Report, TESLA-FEL 95-03, DESY, June 1995; J. Rossbach et al., contribution to the FEL '95 Conference, TESLA-FEL 95-04 and Nucl. Instrum. and Methods **A375** (1996)269.

[3] Laser Handbook, vol. 6. Edited by W.B. Colson, C. Pellegrini, and A. Renieri (North-Holland, 1990).

[4] K.J. Kim and M. Xie, Nucl. Instrum. and Methods **A331** (1993)359.

[5] D.C. Quimby, C.J. Elliott, Nucl. Instrum. and Methods **A296** (1990)451.

[6] B. Faatz et al., contribution to the FEL '95 Conference, TESLA-FEL 95-04.

[7] J.D. Jackson, Classical Electrodynamics (Wiley, New York, 1975).

[8] M.R. Howells and B.M. Kincaid, Proceedings of the NATO Adv. Study Inst., Maratea, 1992; LBL-34751, Sep. 1993.

[9] R.P. Walker and B. Diviacco, Rev. Sci. Instrum. **63 (1)** (1992)392.

[10] R.P. Walker, Nucl. Instrum. and Methods **A267** (1988)537.

[11] W.H. Press et al., Numerical Recipes (Cambridge University, Cambridge, 1986).

[12] D.A. Mossessian and P.A. Heimann, Rev. Sci. Instrum. **66 (11)** (1996)5153.

[13] B.L. Henke et al., Atomic Data and Nucl. Data Tables, **54(2)** (1993) 181. Data also available through WWW at http://grace.lbl.gov/optical_constants/.

[14] R. Klanner, Nucl. Instrum. and Methods **235** (1985)209; G. Hall, Rept. Prog. Phys. **57** (1994)481.

[15] L. Strüder and H. Soltau, Radiation Prot. Dosimetry **61 (1-3)** (1995)39.

[16] P. Lechner and L. Strüder, Nucl. Instrum. and Methods **A354** (1995)464.

[17] E. Gatti and P. Rehak, Nucl. Instrum. and Methods **225** (1984)608.

[18] E. Gatti, P. Rehak, and J.T. Walton, Nucl. Instrum. and Methods **226** (1984)129.

[19] E. Belau *et al.*, Nucl. Instrum. and Methods **214** (1983)253.

[20] V. Radeka, Ann. Review Nucl. Part. Sci., **38** (1988) 217; IEEE, **NS-21** (1974)51; IEEE, **NS-15** (1968) 455.

[21] L. Strüder *et al.*, Nucl. Instrum. and Methods **A288** (1990)227; H. Bräuninger *et al.*, Nucl. Instrum. and Methods **A326** (1993)1239; P. Lechner *et al.*, Nucl. Instrum. and Methods **A326** (1993)284.

[22] E. Pinotti *et al.*, Nucl. Instrum. and Methods **A326** (1993)85;

[23] R.E. Shafer, in AIP Conf. Proc. No. 249, Phys. of Part. Acc., edited by M. Month and M. Dienes (1992).

[24] G. Lutz *et al.*, Nucl. Instrum. and Methods **A263** (1988)163.

[25] W. Blum, H. Kroha, P.Widmann, MPI-PhE/95-13 and Nucl. Instrum. and Methods **A367** (1995)413.

[26] K.C.D. Chan, Nucl. Instrum. and Methods **296** (1990)749; R. Wallace and K.C.D. Chan, Nucl. Instrum. and Methods **304** (1991)400.